

## Performance of the joint LST-1 and MAGIC observations evaluated with Crab Nebula data

H. Abe<sup>1</sup>, K. Abe<sup>2</sup>, S. Abe<sup>1</sup>, V. A. Acciari<sup>3</sup>, A. Aguasca-Cabot<sup>4</sup>, I. Agudo<sup>5</sup>, N. Alvarez Crespo<sup>6</sup>, T. Aniello<sup>7</sup>, S. Ansoldi<sup>8,9</sup>, L. A. Antonelli<sup>10</sup>, C. Aramo<sup>11</sup>, A. Arbet-Engels<sup>12</sup>, C. Arcaro<sup>13</sup>, M. Artero<sup>14</sup>, K. Asano<sup>1</sup>, P. Aubert<sup>15</sup>, D. Baack<sup>16</sup>, A. Babić<sup>17</sup>, A. Baktash<sup>18</sup>, A. Bamba<sup>19</sup>, A. Baquero Larriva<sup>20,21</sup>, L. Baroncelli<sup>22</sup>, U. Barres de Almeida<sup>23</sup>, J. A. Barrio<sup>20</sup>, I. Batković<sup>24</sup>, J. Baxter<sup>1</sup>, J. Becerra González<sup>3</sup>, W. Bednarek<sup>25</sup>, E. Bernardini<sup>24</sup>, M. I. Bernardos<sup>5</sup>, J. Bernete Medrano<sup>26</sup>, A. Berti<sup>12,\*</sup>, J. Besenrieder<sup>12</sup>, P. Bhattacharjee<sup>15</sup>, N. Biederbeck<sup>16</sup>, C. Bigongiari<sup>10</sup>, A. Biland<sup>27</sup>, E. Bissaldi<sup>28</sup>, O. Blanch<sup>14</sup>, G. Bonnoli<sup>29</sup>, P. Bordas<sup>4</sup>, Ž. Bošnjak<sup>17</sup>, A. Bulgarelli<sup>22</sup>, I. Burelli<sup>8</sup>, L. Burmistrov<sup>30</sup>, M. Buscemi<sup>31</sup>, G. Busetto<sup>13</sup>, A. Campoy Ordaz<sup>32</sup>, M. Cardillo<sup>33</sup>, S. Caroff<sup>15</sup>, A. Carosi<sup>10</sup>, R. Carosi<sup>34</sup>, M. S. Carrasco<sup>35</sup>, M. Carretero-Castrillo<sup>4</sup>, F. Cassol<sup>35</sup>, A. J. Castro-Tirado<sup>5</sup>, D. Cauz<sup>8</sup>, D. Cerasole<sup>36</sup>, G. Ceribella<sup>12</sup>, Y. Chai<sup>12</sup>, K. Cheng<sup>1</sup>, A. Chiavassa<sup>37</sup>, M. Chikawa<sup>1</sup>, L. Chytka<sup>38</sup>, A. Cifuentes<sup>26</sup>, S. Cikota<sup>17</sup>, E. Colombo<sup>3</sup>, J. L. Contreras<sup>20</sup>, A. Cornelia<sup>24</sup>, J. Cortina<sup>26</sup>, H. Costantini<sup>35</sup>, S. Covino<sup>7</sup>, G. D'Amico<sup>39</sup>, V. D'Elia<sup>7</sup>, P. Da Vela<sup>34,40</sup>, M. Dalchenko<sup>30</sup>, F. Dazzi<sup>7</sup>, A. De Angelis<sup>13</sup>, M. de Bony de Lavergne<sup>15</sup>, B. De Lotto<sup>8</sup>, M. De Lucia<sup>11</sup>, R. de Menezes<sup>37</sup>, L. Del Peral<sup>41</sup>, A. Del Popolo<sup>42</sup>, G. Deleglise<sup>15</sup>, M. Delfino<sup>14,43</sup>, C. Delgado Mendez<sup>26</sup>, J. Delgado Mengual<sup>44</sup>, D. della Volpe<sup>30</sup>, M. Dellaiera<sup>15</sup>, D. Depaoli<sup>45</sup>, A. De Angelis<sup>24</sup>, A. Di Piano<sup>22</sup>, F. Di Pierro<sup>37,\*</sup>, A. Di Pilato<sup>30</sup>, R. Di Tria<sup>36</sup>, L. Di Venere<sup>36</sup>, R. M. Dominik<sup>16</sup>, D. Dominis Prester<sup>46</sup>, A. Donini<sup>10</sup>, D. Dorner<sup>47</sup>, M. Doro<sup>24</sup>, C. Díaz<sup>26</sup>, L. Eisenberger<sup>47</sup>, D. Elsässer<sup>16</sup>, G. Emery<sup>35</sup>, J. Escudero<sup>5</sup>, V. Fallah Ramazani<sup>48</sup>, L. Fariña<sup>14</sup>, A. Fattorini<sup>16</sup>, G. Ferrara<sup>31</sup>, F. Ferrarotto<sup>49</sup>, A. Fiasson<sup>15,50</sup>, L. Foffano<sup>33</sup>, L. Font<sup>32</sup>, L. Freixas Coromina<sup>26</sup>, S. Fröse<sup>16</sup>, S. Fukami<sup>1</sup>, Y. Fukazawa<sup>51</sup>, R. J. Garcia López<sup>3</sup>, E. Garcia<sup>15</sup>, M. Garczarczyk<sup>52</sup>, R. J. García López<sup>3</sup>, C. Gasbarra<sup>53</sup>, D. Gasparrini<sup>53</sup>, S. Gasparyan<sup>54</sup>, M. Gaug<sup>32</sup>, D. Geyer<sup>16</sup>, J. G. Giesbrecht Paiva<sup>23</sup>, N. Giglietto<sup>28</sup>, F. Giordano<sup>36</sup>, P. Gliwny<sup>25</sup>, N. Godinović<sup>55</sup>, R. Grau<sup>14</sup>, D. Green<sup>12</sup>, J. G. Green<sup>12</sup>, S. Gunji<sup>56</sup>, P. Günther<sup>47</sup>, J. Hackfeld<sup>48</sup>, D. Hadasch<sup>1</sup>, A. Hahn<sup>12</sup>, K. Hashiyama<sup>1</sup>, T. Hassan<sup>26</sup>, K. Hayashi<sup>1</sup>, L. Heckmann<sup>12</sup>, M. Heller<sup>30</sup>, J. Herrera Llorente<sup>3</sup>, K. Hirotani<sup>1</sup>, D. Hoffmann<sup>35</sup>, D. Horns<sup>18</sup>, J. Houles<sup>35</sup>, M. Hrabovsky<sup>38</sup>, D. Hrupec<sup>57</sup>, D. Hui<sup>1</sup>, M. Hütten<sup>1</sup>, M. Iarlori<sup>58</sup>, R. Imazawa<sup>51</sup>, T. Inada<sup>1</sup>, Y. Inoue<sup>1</sup>, K. Ioka<sup>59</sup>, M. Iori<sup>49</sup>, R. Iotov<sup>47</sup>, K. Ishio<sup>25</sup>, M. Jacquemont<sup>15</sup>, I. Jiménez Martínez<sup>26</sup>, E. Jobst<sup>12</sup>, J. Jormanainen<sup>60</sup>, J. Jurysek<sup>61</sup>, M. Kagaya<sup>1</sup>, V. Karas<sup>62</sup>, H. Katagiri<sup>63</sup>, J. Kataoka<sup>64</sup>, D. Kerszberg<sup>14</sup>, G. W. Kluge<sup>39,65</sup>, Y. Kobayashi<sup>1</sup>, K. Kohri<sup>66</sup>, A. Kong<sup>1</sup>, P. M. Kouch<sup>60</sup>, H. Kubo<sup>1</sup>, J. Kushida<sup>2</sup>, M. Lainez<sup>20</sup>, G. Lamanna<sup>15</sup>, A. Lamastra<sup>10</sup>, T. Le Flour<sup>15</sup>, F. Leone<sup>7</sup>, E. Lindfors<sup>60</sup>, L. Linhoff<sup>16</sup>, M. Linhoff<sup>16</sup>, S. Lombardi<sup>7</sup>, F. Longo<sup>67</sup>, S. Loporchio<sup>36</sup>, A. Lorini<sup>68</sup>, J. Lozano Bahilo<sup>41</sup>, P. L. Luque-Escamilla<sup>69</sup>, E. Lyard<sup>70</sup>, M. Láinez Lezáun<sup>20</sup>, R. López-Coto<sup>5</sup>, M. López-Moya<sup>20</sup>, A. López-Oramas<sup>3</sup>, B. Machado de Oliveira Fraga<sup>23</sup>, P. Majumdar<sup>1,71</sup>, M. Makariev<sup>72</sup>, D. Mandat<sup>61</sup>, G. Maneva<sup>72</sup>, M. Manganaro<sup>46</sup>, S. Mangano<sup>26</sup>, N. Mang<sup>16</sup>, G. Manicò<sup>31</sup>, K. Mannheim<sup>47</sup>, M. Mariotti<sup>24</sup>, P. Marquez<sup>14</sup>, G. Marsella<sup>31,73</sup>, O. Martinez<sup>6</sup>, G. Martínez<sup>26</sup>, M. Martínez<sup>14</sup>, J. Martí<sup>69</sup>, A. Mas-Aguilar<sup>20</sup>, G. Maurin<sup>15</sup>, D. Mazin<sup>1,12</sup>, S. Menchiari<sup>74</sup>, S. Mender<sup>16</sup>, E. Mestre Guillen<sup>69</sup>, S. Micanovic<sup>46</sup>, D. Miceli<sup>24</sup>, T. Miener<sup>20</sup>, J. M. Miranda<sup>6</sup>, R. Mirzoyan<sup>12</sup>, T. Mizuno<sup>75</sup>, S. Mićanović<sup>46</sup>, M. Molero González<sup>3</sup>, E. Molina<sup>4</sup>, H. A. Mondal<sup>71</sup>, T. Montaruli<sup>30</sup>, I. Monteiro<sup>15</sup>, A. Moralejo<sup>14</sup>, D. Morcuende<sup>20</sup>, A. Morselli<sup>53</sup>, V. Moya<sup>20</sup>, H. Muraiishi<sup>76</sup>, K. Murase<sup>1</sup>, S. Nagataki<sup>77</sup>, T. Nakamori<sup>56</sup>, C. Nanci<sup>7</sup>, A. Neronov<sup>78</sup>, V. Neustroev<sup>79</sup>, L. Nickel<sup>16</sup>, M. Nievas Rosillo<sup>3</sup>, C. Nigro<sup>14</sup>, L. Nikolić<sup>74</sup>, K. Nilsson<sup>60</sup>, K. Nishijima<sup>2</sup>, T. Njoh Ekoume<sup>3</sup>, K. Noda<sup>1</sup>, D. Nosek<sup>80</sup>, S. Nozaki<sup>12</sup>, M. Ohishi<sup>1</sup>, Y. Ohtani<sup>1,\*</sup>, T. Oka<sup>81</sup>, A. Okumura<sup>82,83</sup>, R. Orito<sup>84</sup>, J. Otero-Santos<sup>3</sup>, S. Paiano<sup>7</sup>, M. Palatiello<sup>8</sup>, D. Paneque<sup>12</sup>, F. R. Pantaleo<sup>28</sup>, R. Paoletti<sup>68</sup>, J. M. Paredes<sup>4</sup>, L. Pavletić<sup>46</sup>, M. Pech<sup>61</sup>, M. Pecimotika<sup>46</sup>, M. Peresano<sup>37</sup>, M. Persic<sup>8,85</sup>, F. Pfeiffle<sup>47</sup>, E. Pietropaolo<sup>58</sup>, M. Pihet<sup>13</sup>, G. Pirola<sup>12</sup>, C. Plard<sup>15</sup>, F. Podobnik<sup>68</sup>, V. Poireau<sup>15</sup>, M. Polo<sup>26</sup>, E. Pons<sup>15</sup>, P. G. Prada Moroni<sup>34</sup>, E. Prandini<sup>24</sup>, J. Prast<sup>15</sup>, G. Principe<sup>67</sup>, C. Priyadarshi<sup>14</sup>, M. Prouza<sup>61</sup>, R. Rando<sup>24</sup>, W. Rhode<sup>16</sup>, M. Ribó<sup>4</sup>, J. Rico<sup>14</sup>, C. Righi<sup>7</sup>, V. Rizi<sup>58</sup>, G. Rodriguez Fernandez<sup>53</sup>, M. D. Rodríguez Frías<sup>41</sup>, N. Sahakyan<sup>54</sup>, T. Saito<sup>1</sup>, S. Sakurai<sup>1</sup>, D. A. Sanchez<sup>15</sup>, K. Satalecka<sup>60</sup>, M. Sato<sup>15</sup>, Y. Sato<sup>86</sup>, F. G. Saturni<sup>10</sup>, V. Savchenko<sup>78</sup>, B. Schleicher<sup>47</sup>, K. Schmidt<sup>16</sup>, F. Schmuckermaier<sup>12</sup>, J. L. Schubert<sup>16</sup>, F. Schussler<sup>87</sup>, T. Schweizer<sup>12</sup>, A. Sciacaluga<sup>7</sup>, T. Siebert<sup>47</sup>, R. Silvia<sup>36</sup>, J. Sitarek<sup>25,\*</sup>, V. Sliushar<sup>70</sup>, D. Sobczynska<sup>25</sup>, A. Spolon<sup>24</sup>, A. Stamerra<sup>7</sup>, J. Strišković<sup>57</sup>, D. Strom<sup>12</sup>, M. Strzys<sup>1</sup>, Y. Suda<sup>51,\*</sup>, S. Suutarinen<sup>60</sup>, T. Šarić<sup>55</sup>, H. Tajima<sup>82</sup>, H. Takahashi<sup>51</sup>, M. Takahashi<sup>82</sup>, J. Takata<sup>1</sup>, R. Takeishi<sup>1</sup>, P. H. T. Tam<sup>1</sup>, S. J. Tanaka<sup>86</sup>, D. Tateishi<sup>88</sup>, F. Tavecchio<sup>7</sup>, P. Temnikov<sup>72</sup>, Y. Terada<sup>88</sup>, K. Terauchi<sup>81</sup>, T. Terzić<sup>46</sup>,

\* Corresponding author: e-mail: [contact.magic@mpp.mpg.de](mailto:contact.magic@mpp.mpg.de); [lst-contact@cta-observatory.org](mailto:lst-contact@cta-observatory.org)

M. Teshima<sup>1,12</sup>, M. Tluczykont<sup>18</sup>, F. Tokanai<sup>56</sup>, D. F. Torres<sup>89</sup>, L. Tosti<sup>90</sup>, P. Travnicek<sup>61</sup>, S. Truzzi<sup>68</sup>, A. Tutone<sup>10</sup>, S. Ubach<sup>32</sup>, M. Vacula<sup>38</sup>, P. Vallania<sup>37</sup>, J. van Scherpenberg<sup>12</sup>, M. Vazquez Acosta<sup>3</sup>, S. Ventura<sup>74</sup>, V. Verguilov<sup>72</sup>, I. Viale<sup>24</sup>, A. Vigliano<sup>8</sup>, C. F. Vigorito<sup>37,91</sup>, E. Visentin<sup>37</sup>, V. Vitale<sup>53</sup>, G. Voutsinas<sup>30</sup>, I. Vovk<sup>1</sup>, T. Vuillaume<sup>15</sup>, M. Vázquez Acosta<sup>3</sup>, R. Walter<sup>70</sup>, Z. Wei<sup>89</sup>, M. Will<sup>12</sup>, T. Yamamoto<sup>92</sup>, R. Yamazaki<sup>86</sup>, T. Yoshida<sup>63</sup>, T. Yoshikoshi<sup>1</sup>, and N. Zywucka<sup>25</sup>

(Affiliations can be found after the references)

Received 17 May 2023 / Accepted 1 October 2023

## ABSTRACT

**Aims.** Large-Sized Telescope 1 (LST-1), the prototype for the Large-Sized Telescope at the upcoming Cherenkov Telescope Array Observatory, is concluding its commissioning phase at the Observatorio del Roque de los Muchachos on the island of La Palma. The proximity of LST-1 to the two MAGIC (Major Atmospheric Gamma Imaging Cherenkov) telescopes makes it possible to carry out observations of the same gamma-ray events with both systems.

**Methods.** We describe the joint LST-1+MAGIC analysis pipeline and used simultaneous Crab Nebula observations and Monte Carlo simulations to assess the performance of the three-telescope system. The addition of the LST-1 telescope allows for the recovery of events in which one of the MAGIC images is too dim to survive analysis quality cuts.

**Results.** Thanks to the resulting increase in the collection area and stronger background rejection, we found a significant improvement in sensitivity, allowing for the detection of 30% weaker fluxes in the energy range between 200 GeV and 3 TeV. The spectrum of the Crab Nebula, reconstructed in the energy range between  $\sim 60$  GeV and  $\sim 10$  TeV, is in agreement with previous measurements.

**Key words.** instrumentation: detectors – methods: data analysis – gamma rays: general

## 1. Introduction

Very-high-energy (VHE  $\gtrsim 100$  GeV) gamma rays cannot be observed directly in an efficient way due to their absorption by the atmosphere. In turn, observations with space-born instrument are marred by relatively low fluxes at those energies. In the last three decades, imaging atmospheric Cherenkov telescopes (IACTs) have proven useful as sensitive instruments in the study of VHE gamma-ray emission from cosmic sources (see e.g., Sitarek 2022 for a recent review). The combination of multiple telescopes at distances on the order of 100 m (comparable to the size of the gamma-ray Cherenkov light pool) allows for joint stereoscopic analyses of the events, thereby improving the performance of the system significantly (Kohnle et al. 1996).

The Cherenkov Telescope Array Observatory (CTAO) is an upcoming next-generation gamma-ray facility (Acharya et al. 2013), composed of two telescope arrays located in the Northern and Southern hemispheres. In order to cover a broad energy range (from a few tens of GeVs up to a few hundreds of TeVs), it is to be composed of telescopes of three different sizes: Large-Sized Telescopes (LSTs), Medium-Sized Telescopes (MSTs), and Small-Sized Telescopes (SSTs). The LSTs, with mirror diameters of 23 m, will be the most sensitive part of the system for the lowest energy range of CTAO (tens of GeV). The construction of the first LST telescope, named LST-1, was completed in October 2018. Since 2019, it has been receiving commissioning and engineering data (CTA-LST project 2021). It is located in Observatorio Roque de los Muchachos, La Palma (Spain), at the altitude of 2200 m a.s.l. It is set at a distance of only  $\sim 100$  m from the MAGIC (Major Atmospheric Gamma Imaging Cherenkov) telescopes, a pair of 17 m IACTs (Aleksić et al. 2016a). Both systems work independently, but their proximity allows for offline searches of common events and enables joint LST-1+MAGIC analysis. A similar array containing telescopes of different sizes is being operated by the H.E.S.S. Collaboration (Holler et al. 2015). However, in that case, the difference in mirror area (approximately by a factor of 5) causes a similar difference in the energy threshold. On the other hand, in the case of LST-1+MAGIC combination, the difference between

the mirror area of the LST-1 and that of the MAGIC telescopes is only a factor of 2.

In this work, we report the common analysis chain of both instruments and its achieved performance using both Monte Carlo (MC) simulations and observations of the Crab Nebula. In Sect. 2, we describe both participating instruments. The applied data and Monte Carlo (MC) simulations are described in Sect. 3. We derive various performance parameters of the joint system and present them in Sect. 4. Our concluding remarks are given in Sect. 5.

## 2. Instruments and data analysis

The relative location of the LST-1 and the MAGIC telescopes, along with their basic parameters are compared in Fig. 1 and Table 1, respectively. While the telescopes have their main design concepts in common, there are some differences, such as the larger LST-1 mirror area, the higher quantum efficiency (QE) of its optical detectors, and its larger field of view (FoV). Despite the same parabolic dish shape (minimizing the time spread of the registered Cherenkov photons) LST-1 has larger f/d and larger camera FoV. The higher event rate in the case of LST-1 is a sum of multiple effects: lower threshold (due to higher QE and mirror area), larger size of the trigger region, and monoscopic operations.

### 2.1. MAGIC

MAGIC is a system made up of two IACTs, separated by a distance of 85 m. The first telescope, MAGIC-I (M1), was constructed in 2003, while MAGIC-II (M2) was added in 2009. Since then, both telescopes have operated in a stereoscopic observation mode (Aleksić et al. 2012). In the standard operation mode, only events triggering both telescopes are saved. The telescopes have undergone a few upgrades (with the most recent in 2012) and since then they share a nearly identical design and comparable performance. While the nominal camera FoV is  $3.5^\circ$ , the part covered by the trigger is limited only to the

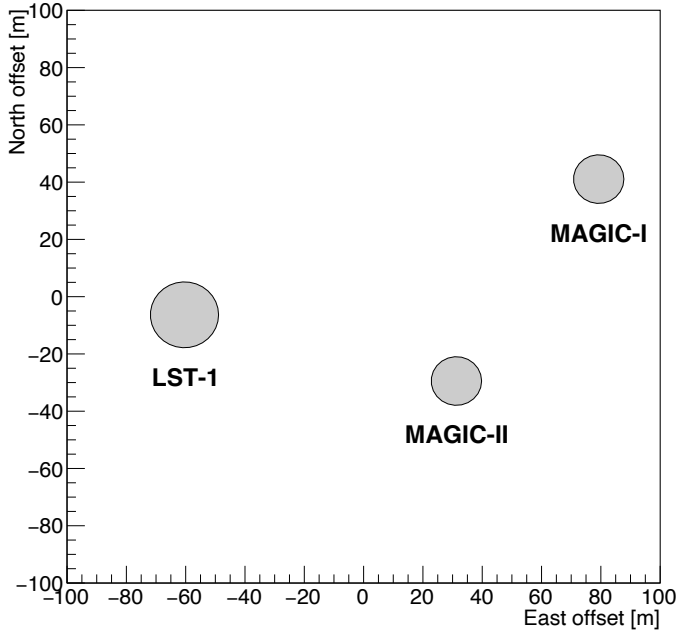


**Fig. 1.** Location of the LST-1 and MAGIC telescopes. The  $X$  and  $Y$  axes represent the geographical East and North direction, respectively. The diameter of the circle is equal to the diameter of the telescope’s mirror dish.

**Table 1.** Comparison of LST-1 and MAGIC telescopes parameters.

Parameter	LST-1	MAGIC I/II
Diameter (d)	23 m	17 m
Focal length (f)	28 m	17 m
Dish shape	Parabolic	Parabolic
Camera FoV	4.5°	3.5°
Pixel FoV	0.1°	0.1°
Number of pixels	1855	1039
Peak QE	41%	32–34%
Sampling speed	1 GHz	1.64 GHz
Trigger type	Mono	Stereo
Typical event rate	10 <sup>4</sup> s <sup>-1</sup>	300 s <sup>-1</sup>
Readout dead time	7 μs	26 μs

inner half of the full camera area. At low zenith angle distance, the energy threshold (defined as the peak of the differential true energy distribution) at trigger level of the MAGIC telescopes for a source with a  $-2.6$  spectral index is  $\sim 50$  GeV (Aleksić et al. 2016b) for a standard digital trigger.

## 2.2. LST-1

LST-1 is the first of the four LSTs to be constructed in the CTAO Northern site (CTA-LST Project 2022). The construction of LST-1 was completed in October 2018, after which its commissioning and validation period started. Currently, the telescope is performing both commissioning and scientific observations. The mirror area being twice as large, as well as the improved QE of the optical sensors (photomultipliers) compared to MAGIC, enable LST-1 to achieve an energy threshold of  $\sim 20$  GeV (Abe et al. 2023). However, as any IACT operating standalone, LST-1 suffers from a huge hadronic background, which is much more efficiently rejected in stereoscopic systems. Similarly, it also has

worse accuracy in terms of the reconstructed shower geometry, which affects the angular and energy resolutions. Therefore, despite the larger light collection, at energies above 100 GeV, the sensitivity of LST-1 alone is a factor  $\sim 1.5$  worse than that of MAGIC (Abe et al. 2023).

## 2.3. Event matching

Currently MAGIC and LST-1 operate independently. Both systems are however equipped with GPS clocks that provide time stamps for each event. Those time stamps can be used for offline matching of events that originate from the same shower (similar approach has been used in the first H.E.S.S. stereoscopic data, H.E.S.S. Collaboration 2006). Due to the different electronic pathways and different travel times of the Cherenkov light to individual telescopes, a pointing-dependent time delay between the arrival times at MAGIC and at LST-1 needs to be taken into account. For each subrun (corresponding to about 10 s of LST-1 data), we match the events with a coincidence window of 0.6 μs. The optimal delay is obtained using an iterative procedure. To also allow for the analysis of LST-1+M1 or LST-1+M2 event types, the procedure is done independently using time stamps in each of the MAGIC telescopes. For the typical rate of LST-1 and MAGIC (see Table 1), this procedure would result in a negligible rate of accidental coincidences of  $\leq 1.8$  s<sup>-1</sup>. Anomalous coincidence combinations (e.g., matching two LST-1 events to one MAGIC event or two MAGIC events to one LST-1 event) were excluded from the data stream; however, they are very rare due to LST-1 and MAGIC deadtimes.

## 2.4. Data analysis

In their standalone operations, both MAGIC and LST-1 use independent analysis chains. The MAGIC data analysis is based on MARS (Moralejo et al. 2009; Zanin et al. 2013), a C++, ROOT-based library, and a package of analysis programs. The raw data are stored in a custom binary format and the data are generated at each processing step are stored using ROOT containers.

On the other hand LST-1 is using `cta-lstchain` (Lopez-Coto et al. 2022), a Python-based analysis library exploiting `ctapipe` (Kosack et al. 2022). The LST-1 raw data consist of pixel-wise waveforms and auxiliary information. They are stored in a `zfits` format (Pence et al. 2012; Lyard et al. 2017) and processed data are stored in HDF5 files (Nozaki et al. 2020).

For the data obtained by observations, we performed the first stages of the data processing, namely the signal extraction from individual pixel waveforms and the calibration of the resulting images to photoelectrons (p.e.) and individual pixel timing, with the specific software of each instrument. Then the MAGIC data are converted into HDF5 format, compatible with the LST-1 data using the dedicated `ctapipe_io_magic` package<sup>1</sup>. The rest of the analysis chain is performed with the `magic-cta-pipe`<sup>2</sup> package using `lstchain` and `ctapipe` methods. In particular, the `magic-cta-pipe` contains analysis scripts to, for example, apply the same image cleaning as in the MARS package, but within a `ctapipe`-like environment and to match the events produced by the same shower in the three telescopes. All the other higher-level analysis steps are performed with the `magic-cta-pipe` package as well, with the help of other modules for specific tasks (e.g., `pyirf`, Noethe et al. 2022, for the calculation of instrument response function, IRF; and

<sup>1</sup> [https://github.com/cta-observatory/ctapipe\\_io\\_magic](https://github.com/cta-observatory/ctapipe_io_magic)

<sup>2</sup> <https://github.com/cta-observatory/magic-cta-pipe>

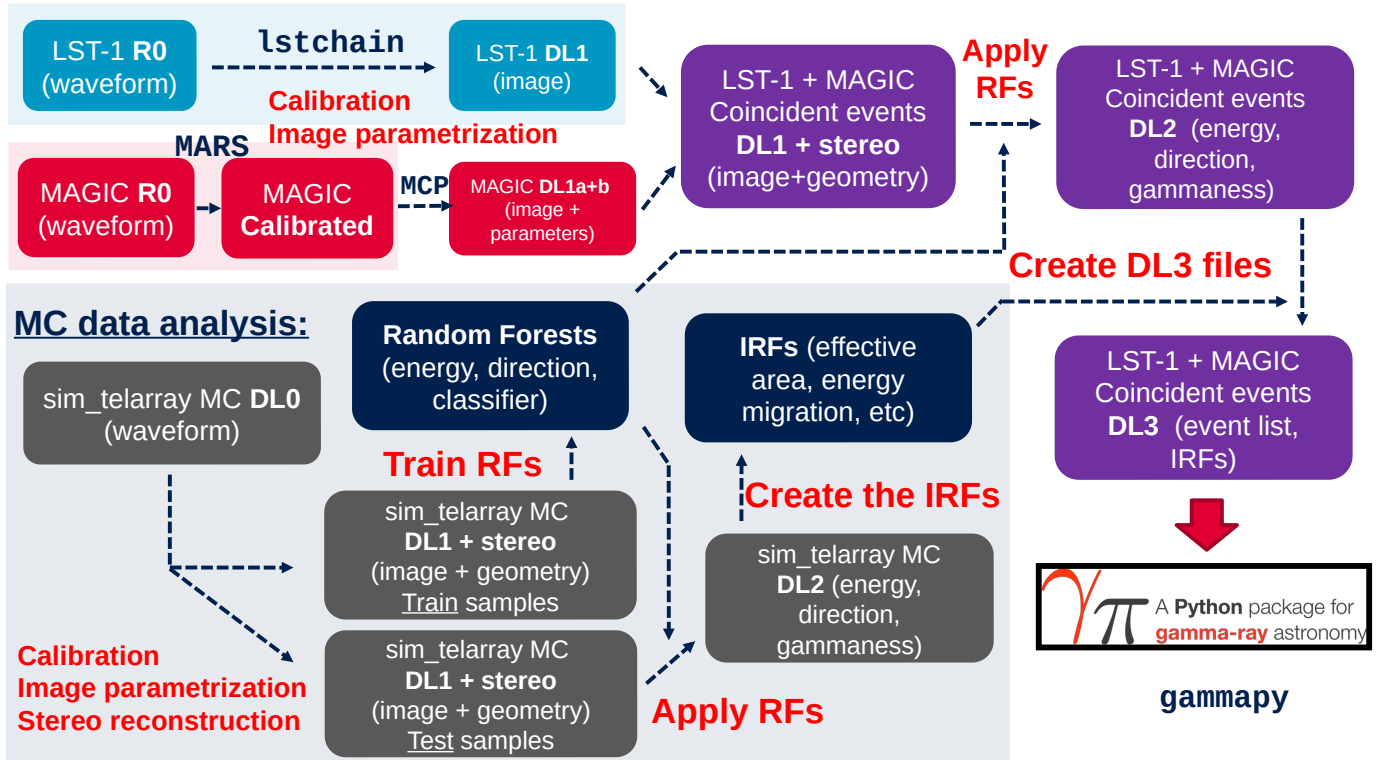


**Fig. 2.** Schematic view of MCP analysis chain. Blue, red, violet, and gray boxed represent different stages of LST-1 data, MAGIC data, joint data, and MC simulations, respectively. Black boxes mark the auxiliary files.

`gammapy`, Deil et al. 2017, for flux estimation). For MC simulations, all the processing (including the calibration) is instead performed with `magic-cta-pipe`. The analysis chain presented in this paper is referred to as the MAGIC-ctapipe (MCP) chain (and summarized in Fig. 2). Such a scheme allows us to take advantage of the automatic processing of the bulky, early stages of data and exploit the already implemented low-level calibration corrections (see e.g., Sitarek et al. 2013 for the case of MAGIC and Cassol et al., in prep. for LST-1). At the same time, it allows for the utilization of state-of-the-art software developed for CTAO, and in turn, the newly developed tools can also be easily applied for CTAO analysis in the future.

After the initial image cleaning (see Aleksić et al. 2016b), the images are parametrized using the classical approach of (Hillas 1985) and a quality cut on “intensity” is applied (i.e., the total number of p.e. in the image should be at least 50 p.e.)<sup>3</sup>. Next, the events are divided into different classes, depending on which telescopes are triggered. We considered the following combinations: M1+M2, LST-1+M1, LST-1+M2, and LST-1+M1+M2. However, it should be noted, that due to the stereoscopic trigger of the MAGIC telescopes, the event types LST-1+M1 and LST-1+M2 also correspond to events in which all three telescopes had been triggered. Though in those events, one of the MAGIC telescopes provided an image that either did not survive the cleaning or had an intensity that was too low. In Table 2, we report the percentage of events of each kind for various data and MC samples (the parameters of the MC simulations are given in Table 3). The dominating type of events are three-telescope events (3/4 of all gamma-ray events). The fraction of LST-1+M2 events is about twice as large as those of LST-1+M1 and this is related to the proximity of LST-1 to the M2 telescope. While

<sup>3</sup> This is a standard cut both in MAGIC and LST-1 analysis chains, see Aleksić et al. (2016b); Abe et al. (2023).

**Table 2.** Percentage of different event types in different types of MC simulations and in the observations.

Type	MC $\gamma$ (0.4°)	MC $\gamma$ (0–2.5°)	MC p	Observations
M1+M2	6.2%	4.8%	20.4%	21.5%
LST-1+M1	7.1%	7.7%	6.2%	5.3%
LST-1+M2	12.5%	12.6%	11.9%	14.2%
LST-1+M1+M2	74.1%	74.8%	61.5%	59.0%

**Notes.** Only images surviving 50 p.e. cut in intensity are considered. Observations and MC simulations cover low zenith distance angle ( $<30^\circ$ ). Proton MC are weighted to  $-2.7$  spectral index, while gamma-ray MC to  $-2.6$ . Values for gamma-ray simulations are provided separated for showers at typical offset from the pointing direction (0.4°) and for isotropic distribution (within  $2.5^\circ$  from the pointing direction).

the percentages of different event types in proton simulations roughly follow what has been observed in the data, there are some minor differences at (absolute) 1–2% level. They are likely caused by the presence of helium and higher elements in the data, as well as incompleteness of the simulations due to very large impact and offset angle events. Additionally, the regular systematic effects (light yield, optical points spread function, etc.) causing slight MC-data mismatches can also contribute to those small differences. The fraction of MAGIC-only (without the LST-1 counterpart) events is significantly larger in the observations and in the proton MC simulations ( $\sim 20\%$ ) compared to the gamma-ray MC simulations ( $\sim 5\text{--}6\%$ , comparable for both point-like and diffuse gamma-ray simulations). We interpret this as a result of intrinsic differences between the Cherenkov light

**Table 3.** Summary of the generated MC samples and their zenith distance range, energy range, maximum impact parameter, and viewcone (maximum offset angle from the camera center).

Sample	Particle type	$Zd$ [°]	$E_{\min}$ [GeV]	$E_{\max}$ [TeV]	$\text{Impact}_{\max}$ [m]	Viewcone [°]
Train	Gamma	6–52	$5 \times \cos^{-2.5} Zd$	$50 \times \cos^{-2.5} Zd$	$900 \times \cos^{-0.5} Zd$	0–2.5
	Protons	6–52	$10 \times \cos^{-2.5} Zd$	$\min(100 \times \cos^{-2.5} Zd, 200)$	$1500 \times \cos^{-0.5} Zd$	$0-8 \times \cos^{0.5} Zd$
Test	Gamma	10–55	$5 \times \cos^{-2.5} Zd$	$50 \times \cos^{-2.5} Zd$	$700 \times \cos^{-0.5} Zd$	0.4
	helium	10–43	$20 \times \cos^{-1.5} Zd$	$200 \times \cos^{-1.5} Zd$	$1500 \times \cos^{-1} Zd$	0–8
	Electrons	10–43	$5 \times \cos^{-2.5} Zd$	$50 \times \cos^{-2.5} Zd$	720–1200	0–7.5

**Notes.** The first three samples are the same as those used in Abe et al. (2023).

distribution on the ground for showers initiated by different primary particles. Gamma-ray-induced events have in general a smooth Cherenkov photon distribution on the ground. For such “regular” events, if they are bright enough to be detected by both MAGIC telescopes, the significantly higher light yield of LST-1 normally also allows for the detection of the shower by the third telescope. However, hadronic events show irregularities in their ground distribution of Cherenkov light, caused by individual high transverse momentum sub-showers. Such events can produce a significant signal in MAGIC telescopes without an LST-1 event counterpart. Considering the small fraction of MAGIC-only events, and their dominant background origin, we excluded those events from further analysis.

For convenience, as well as to exploit the information of telescopes not containing the image, the events were then divided into the combination types (see Table 2). For each event type and telescope participating in the combination, the gamma-hadron separation parameter (i.e., “gammaness”, see Abe et al. 2023), estimated energy, and the estimated *DISP* parameter (estimated distance of the source position projected on the camera to the centroid of the image, Lessard et al. 2001; Aleksić et al. 2010) were computed. The training was done using a random forest (RF) method (Breiman 2001), implemented in the *scikit-learn* package (Pedregosa et al. 2011). The RF regressors used for energy and *DISP* estimations used 150 estimators, a maximum tree depth of 50, the squared error criterion for selection of the best cut from all the parameters at each step and division of leaves down to a single event. The RF classifier used for gamma-hadron separation employed 100 estimators with a maximum depth of 100. In this case, the RF branching was done using the Gini index criterion, but at each step, only the square root of the total number of parameters is randomly selected. Individual telescope estimates are based on the Hillas parametrization (intensity, length, width, skewness, kurtosis, and time slope computed along the main axis of the image, and fraction of total image intensity in the two outermost rings of pixels) in the particular telescope. In each telescope, this information is combined with tentative stereoscopic parameters obtained from the axis crossing method (Hofmann et al. 1999) (height of the shower maximum, impact parameter) and pointing direction (azimuth and zenith distance angles). In order to obtain event-wise classifiers and estimators, the individual telescope responses are weighted with the image intensity<sup>4</sup>. In this way, brighter and better-reconstructed images are favored in the final estimation.

<sup>4</sup> Other possible weights, including inverse of variance of the response of individual trees, were tested and proved comparable, but led to a slightly worse performance.

A special averaging procedure was applied for the estimation of the arrival direction of the shower. The arrival direction can be reconstructed from an image using the *DISP* parameter, assuming that it lies on the main axis of the image in the camera plane. There are, however, two directions that fulfill this condition, located on opposite sides of the image. The selection of the correct one (the so-called head-tail discrimination), especially at the lower energies, may fail in a fraction of events. For example, Abe et al. 2023 reports that approximately 20% of all gamma-ray events have head and tail wrongly discriminated for a spectrum similar to the Crab Nebula<sup>5</sup>.

Therefore, we applied the Stereo *DISP* RF method (Aleksić et al. 2016b), adapted to three-telescopes observations. Specifically, we scanned all possible combinations of pairs of possible arrival directions from individual images and select the one that yields the smallest spread of reconstructed positions. The spread is quantified with the *disp\_diff\_mean* parameter, defined as the sum of angular distances of reconstructed directions from all pairs of telescopes, divided by the number of such pairs. In order to enhance the angular resolution and provide additional rejection of hadronic events (which are more likely to have irregular images), we apply an additional cut of *disp\_diff\_mean* < 0.22°. The same value of the cut is used in the standard MARS analysis chain. The change of collection area at different stages of analysis (including application of the quality cuts) is summarized and discussed in Appendix A.

### 2.5. Simulations of the telescopes’ response to showers

To train the shower reconstruction algorithm and to evaluate IRFs, the analysis of IACT data requires MC simulations. In the case of LST-1, the development of showers is simulated using CORSIKA (Heck et al. 1998), while the response of the telescope is simulated with the *sim\_telarray* program (Bernlöhr 2008). On the other hand, within MAGIC, MC simulations of showers are generated using a slightly modified version of CORSIKA, but the response of the telescopes is obtained using *MagicSoft* programs (*reflector* and *camera*; Majumdar et al. 2005). Common LST-1+MAGIC observations require the analysis chain to be performed within the same framework, and the same should happen for the simulations.

We performed simulations of the same showers visible by both MAGIC and LST-1, using the *sim\_telarray* program. To achieve this, we translated the simulation parameters of the

<sup>5</sup> This fraction was obtained after cleaning, an intensity cut of 50 p.e., and with the main image axis oriented within 0.3° of the nominal source position. It is, however, strongly dependent on energy, dropping below 5% above 200 GeV.

MAGIC telescopes from the reflector and camera simulation programs into the `sim_telarray` nomenclature. For most of the parameters (e.g., mirror dish geometry, angular dependence of light guide efficiencies, average quantum efficiency of PMT, jitter of single p.e. times, telescope trigger parameters, and read-out pulse shape), the translation was direct and the same values and curves were used in both simulation chains. For some of the parameters, however, minor simplifications or averaging had to be applied due to intrinsic differences between the two softwares. For example, this was the case for the simulation of the mirrors reflectivity and the noise within the pulse integration window. Thanks to the usage of `sim_telarray`, the LST-1 simulation parameters could be taken directly from the standard configuration, the so-called LSTProd2 (as in Abe et al. 2023). The common parameters (atmospheric model, geomagnetic field) follow the LSTProd2 settings. The level of uniform night sky background (NSB) was adjusted at the analysis level in the case of LST-1, following the procedure described in Abe et al. (2023). In the case of MAGIC, the adjustment was done according to the same principle (matching noise in empty, the so-called pedestal, and events), but already at the telescope camera response simulation level. The validation process of the MC simulation settings on a dedicated MC production is described in Appendix B. As a final end-to-end check, we also compared the energies of MAGIC events reconstructed with both the MCP (based on the `sim_telarray` MCs) and MARS (based on standard MAGIC MCs) chains, achieving similar accuracy (see Appendix C).

### 3. Observation and simulation samples

We determined the performance of the joint analysis chain in two ways: first using observation data taken from the direction of the Crab Nebula and then using dedicated MC simulations.

#### 3.1. Observations

In order to evaluate the performance of the joint analysis, we used 4 h of good-quality Crab Nebula data taken simultaneously by the LST-1 and MAGIC telescopes. The observations span the period between October 2020 and March 2021, and taken in wobble observation mode, with the source position offset by  $0.4^\circ$  from the camera center. After every 20-min long run, the direction of the offset was flipped to maintain consistency between the source and the background control region. Only data in which the pointing direction of both systems matched within  $0.1^\circ$  were used. The data was taken at low and medium zenith angles, namely 0.8 h in between  $12^\circ$ – $30^\circ$ , 2.3 h in  $30^\circ$ – $45^\circ$  and 0.6 h in between  $45^\circ$ – $53^\circ$ .

#### 3.2. MC simulations

For most of the analysis chain we re-use the same MC simulation samples of protons and gamma rays as in Abe et al. (2023). However, we also used additional simulations of helium and electrons, with reoptimized scaling of the simulation parameters (maximum impact parameter and offset angle from the camera center) with zenith angle distance, to improve the sample completeness. The samples were generated at fixed pointings along the path of the source in the sky (training samples), or to cover the full-sky on a grid of pointings (test samples), see Abe et al. (2023) for details. All the MC samples are generated with spectral index of  $-2$  and reweighted to specific particle spectra. The productions are summarized in Table 3. In the interest of studying the performance with MC as well,

we divided the “TrainProton” sample into training and testing sub-samples.

#### 3.3. Data/MC comparisons

To ensure the correct reproduction of observed data by the MC simulations, we performed an end-to-end comparison with the data. As the gamma-ray showers are more regular and (on average) less extended than hadronic ones, comparisons performed with gamma-ray events are sensitive to possible data-MC mismatches. Hence, we present a comparison with selected gamma-ray events, which also reflect the performance for gamma-ray observations. Nevertheless, for completeness of the study and to validate the analysis threshold, we also performed similar comparisons with the background events (see Appendix D).

We derived the parameter distributions obtained from the gamma-ray excess events. The distributions are extracted from Crab Nebula observations after subtraction of the residual background using a background control region. We compared these excess distributions to the simulated gamma rays weighted (and normalized) according to the spectrum that was measured by Aleksić et al. (2015). In this approach, the gamma-ray events are dominated by a background of much more abundant hadronic showers. Thus, to avoid large statistical (and systematic) errors, some kind of background suppression needs to be applied. In order to perform the comparison without introducing a large bias, we applied soft cuts corresponding to 95% “gammaness” efficiency (in each estimated energy bin), and considered only events with reconstructed direction up to  $0.2^\circ$  away from the nominal source position.

The results of the comparison are shown in Fig. 3. The “intensity” distribution is roughly reproduced. We note that the MC simulation shape of the distribution of these parameters (in particular, the intensity) is dependent on the assumed spectral model of the Crab Nebula. The length distribution is well matching between the data and MCs. However, contrary to the background case (cf. Appendix D), the width parameter is slightly underestimated in the case of MAGIC-I and MAGIC-II telescopes, which could be for instance due to insufficiently accurate simulations of the optical PSF. Despite this, the “gammaness” distribution, both for individual telescopes and average, is still sufficiently well reproduced in the simulations to avoid introducing large systematic errors. The reconstructed height of the shower maximum is slightly shifted towards higher values in MC simulations than in the data. This could be due to a combination of various effects, for instance: a systematic uncertainty on the energy scale of the telescopes, a mismatch between the zenith and azimuth distributions, which are continuous for the data and discrete for the simulations, or a slight mispointing of the telescopes. Finally, while the reconstruction of the event direction is roughly consistent with the simulations, a slight increase of the high-values tail in the data is present as well. Similarly, a slight mismatch in such distributions has been observed in LST-1-alone and MAGIC-alone observations, and might be related to arcmin-scale mispointing of the telescopes (Aleksić et al. 2016b; Abe et al. 2023).

### 4. Performance parameters

Using Crab Nebula data and MC simulations, we evaluated various performance parameters of the joint analysis chain and compared those with the MAGIC-only analysis. We also compared

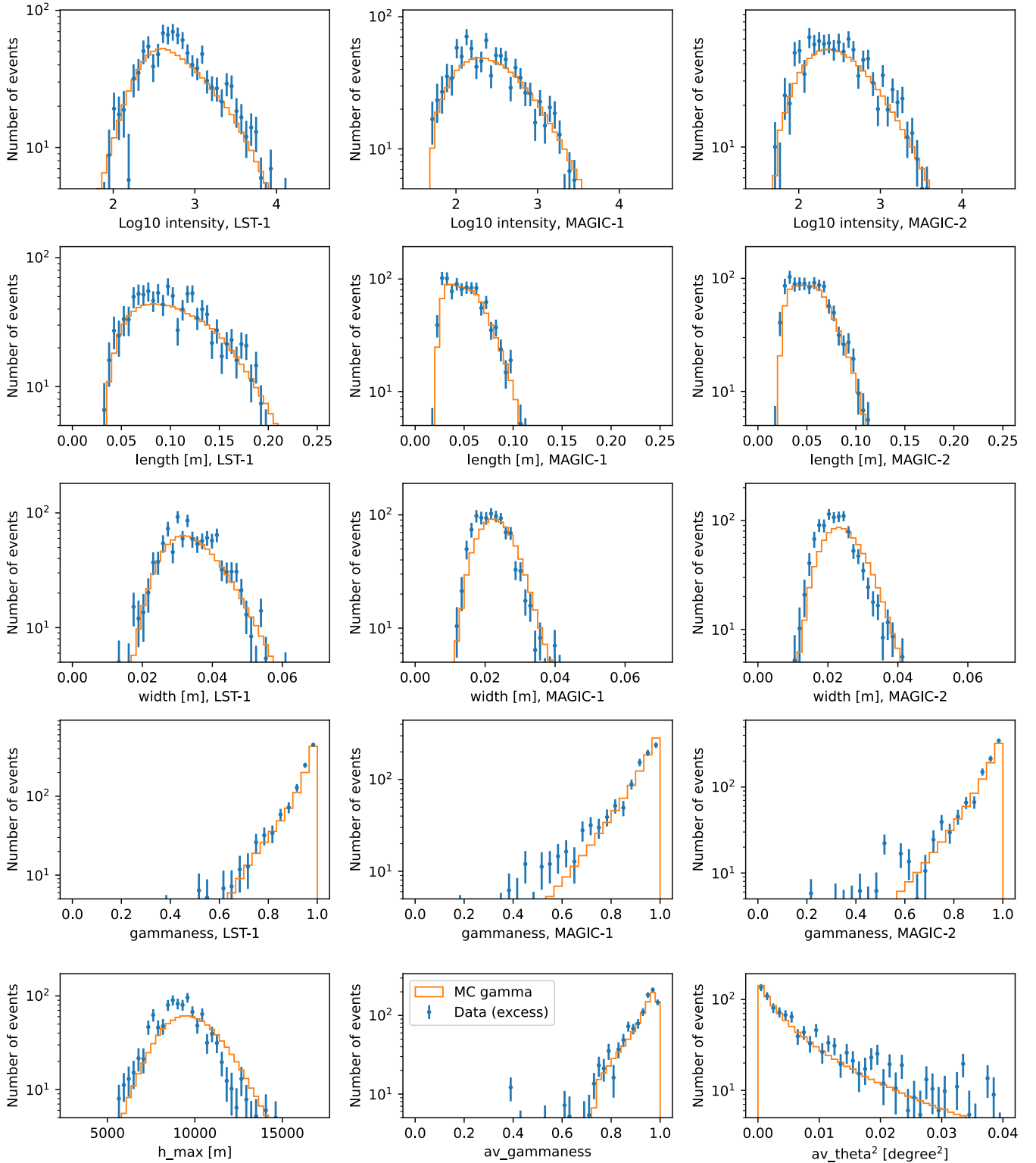


**Fig. 3.** Comparison of image parameters between the gamma-ray excess in the data (blue) and MC simulations of gamma rays (orange). Only observations with zenith distance below  $30^\circ$  are used. The top four rows of panels show intensity, length, width, and individual telescope “gammaness” (from top to bottom) for LST-1 (left), MAGIC-I (middle), and MAGIC-II (right). The bottom row shows stereoscopic parameters: height of the shower maximum (left), averaged “gammaness” (middle) and squared reconstructed distance to the source (right).

the sensitivity and flux reconstruction with the LST-1-only analysis. As the performance of Cherenkov telescopes is strongly dependent on the zenith distance of the pointing, we investigated the case of  $Zd < 30^\circ$  and  $30^\circ < Zd < 45^\circ$  separately to provide a comparison with the MAGIC-only performance.

#### 4.1. Energy threshold

In Fig. 4, we present the differential true energy distribution for a source with a  $-2.6$  spectrum. In the case of MAGIC-only events, the energy threshold (peak position of that distribution) at the

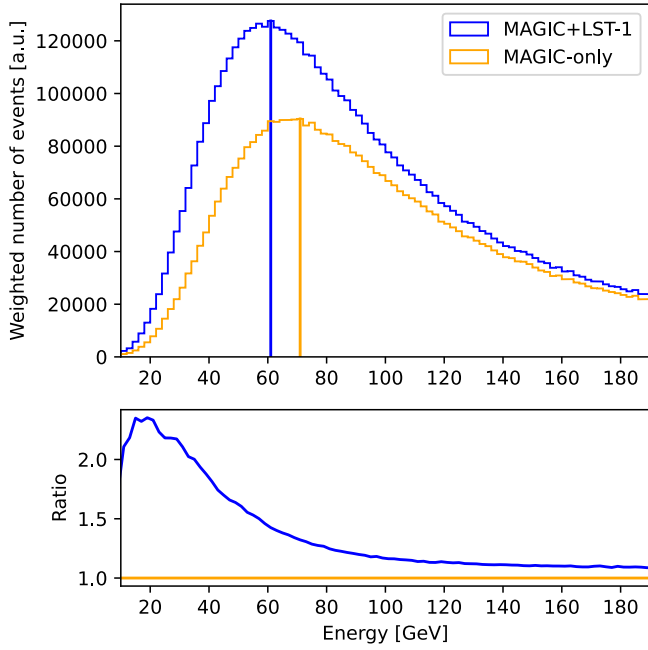


**Fig. 4.** True energy distribution obtained with MC simulations (weighted to a source spectrum of  $-2.6$ ) of gamma rays for  $Zd < 30^\circ$  at the reconstruction level (at least two images with an intensity of  $>50$ ). Vertical lines show the peak position for the joint analysis (blue) and MAGIC-only analysis (orange). Bottom panel shows the ratio of the two curves.

stereoscopic reconstruction level of  $\sim 70$  GeV is consistent with the value obtained in [Aleksić et al. \(2016b\)](#). The addition of the third telescope, while it cannot provide additional events at the trigger level, can recover events in which one of the MAGIC images displays an intensity level that is too low for further stereoscopic reconstruction. As a result, the energy threshold at the reconstruction level is reduced to  $\sim 60$  GeV. Additionally, the collection area below the energy threshold is greatly improved, by a factor of about 2 at 30 GeV.

#### 4.2. Flux reconstruction

Since all the data used in this work were taken before August 2021, following [Abe et al. \(2023\)](#), for the spectral analysis we apply an increased cut for the intensity of  $>80$  p.e. for LST-1 images. Due to the significantly larger light yield of LST-1 compared to MAGIC, the effect of this cut on the stereoscopic analysis is very small (e.g., for low zenith angle observations at 30 GeV only 10% of events are removed). For MAGIC images, a standard intensity of  $>50$  p.e. quality cut was applied. To reconstruct the spectrum of the Crab Nebula, we derived the IRFs for a number of simulated azimuth and zenith pointings close to those followed by the source during the observations. To evaluate the IRFs corresponding to individual data runs we employ interpolation. We then divided the sample into an ascending and descending branch (i.e., before and after the culmination). For each branch separately, we performed a one-dimensional (1D) interpolation (over the cosine of zenith distance angle) of the IRFs. Subsequently a global, binned, joint likelihood spectral fit was performed with `gammapy 0.20.1` ([Deil et al. 2017](#); [Donath et al. 2022](#)) to determine the best parameters of the spectral model for a point-like source at the nominal position of the Crab Nebula. Next, the same software was used to derive individual spectral points by fitting the normalization of the global

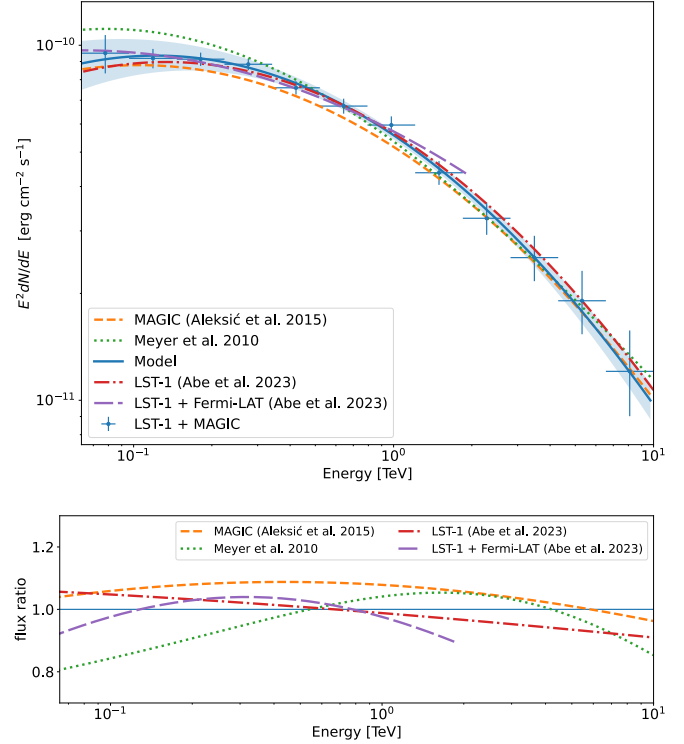


**Fig. 5.** Spectral energy distribution of Crab Nebula obtained with joint LST-1+MAGIC analysis (blue points and fit line, with the statistical uncertainty of the fit shown as shaded region) compared to reference measurements from MAGIC-alone (orange dashed line, [Aleksić et al. 2015](#)), LST-1-alone (red dot-dashed, [Abe et al. 2023](#)), *Fermi*-LAT+LST-1 (violet long-dashed, [Abe et al. 2023](#)), and *Fermi*-LAT+IACT (green dotted line, [Meyer et al. 2010](#)). The bottom panel shows the ratio of the spectral model derived with the joint analysis to the individual reference spectra (see the legend).

model in energy bands. In [Fig. 5](#), we present the resulting spectral energy distribution reconstructed between  $\sim 60$  GeV and  $\sim 10$  TeV from the total investigated data set. The spectrum is modeled in `gammapy` with a log parabola spectrum defined as:

$$dN/dE = A(E/E_0)^{-\alpha-\beta \ln(E/E_0)}, \quad (1)$$

with  $A = (3.48 \pm 0.09_{\text{stat}}) \times 10^{-11} \text{ cm}^{-2} \text{ s}^{-1} \text{ TeV}^{-1}$ ,  $E_0 = 1 \text{ TeV}$ ,  $\alpha = 2.49 \pm 0.03_{\text{stat}}$ ,  $\beta = 0.117 \pm 0.017_{\text{stat}}$ <sup>6</sup>. The resulting spectrum is consistent with previous MAGIC and LST-1 measurements within  $\sim 10\%$ .

In order to evaluate the stability of the flux reconstruction, we computed the light curve of the observed flux above 300 GeV (see [Fig. 6](#)). In the figure, the plotted data are binned night-by-night, however, we also investigated the stability of the flux at the run-by-run (corresponding to  $\leq 20$  min per bin) time scales. Similarly to other IACT measurements ([Aharonian et al. 2006](#); [Aleksić et al. 2016b](#); [Abe et al. 2023](#)), the resulting Crab Nebula light curve is not consistent with a constant fit ( $\chi^2/N_{\text{dof}} = 39.5/15$  for the run-by-run calculations and  $13.1/5$  for night-by-night). Such an observed instability of the flux is likely due to the systematic effects related to, for instance, the atmosphere varying during the observations. We investigated how the  $\chi^2/N_{\text{dof}}$  statistics changes when a given level of systematic uncertainties is added in quadrature to the statistical uncertainty. To achieve

<sup>6</sup> Note: in [Aleksić et al. \(2016b\)](#) the log parabola is defined using the base 10 logarithm, which explains the very different values reported for the  $\beta$  parameter.

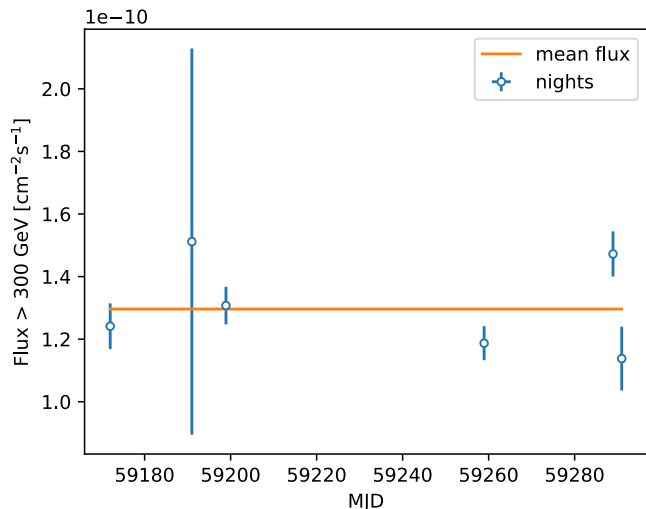


**Fig. 6.** Integral flux of Crab Nebula obtained with joint LST-1+MAGIC analysis binned day-by-day (blue empty points). The horizontal line shows the corresponding average flux from the integrated spectral model.

the corresponding fit probability of 0.5, an additional 12.7% systematic uncertainty is required in the case of run-by-run analysis, as well as 7.9% in the case of night-by-night, which is at the level or even lower than what was estimated for MAGIC.

#### 4.3. Differential flux sensitivity

Sensitivity is a measure of the minimum flux of a source that can be detected with an instrument in a given time exposure. In the case of differential sensitivity, the detection should be achieved independently in a particular energy bin. We followed the definition typically used in the IACT community, namely, the data are divided into 5 bins per decade of reconstructed energy and the event statistics are rescaled to 50 h of observation time. The sensitivity in a given bin then corresponds to the gamma-ray flux from a point-like source that provides  $5\sigma$  significance signal, as computed via Eq. (17) of Li & Ma (1983), with additional two conditions: the number of excess events should be greater than ten and also larger than 5% of the residual background. In the calculations of the significance, we assume that the background can be computed from five regions with the same acceptance of the signal region.

In order to optimize the usage of statistics, we applied a k-fold cross-validation procedure (see e.g., Mosteller & Tukey 1968). Specifically, the sample is divided into four sub-samples, each of them using every fourth event in the sample. For each of them, we apply cuts in arrival direction and “gammaness”, computed using the remaining sub-samples and optimized to provide the best sensitivity. We then stack the events from all sub-samples and compute the final sensitivity that is not biased by the cut selection.

We estimated the sensitivity both with the Crab Nebula data and also with MC simulations. In the latter case, we used the spectrum derived by Aleksić et al. (2015) to convert the flux into Crab Nebula units (C.U.). In the calculations we assume the proton flux of Yue et al. (2019) and the electron flux is a parametrized combination of Fermi-LAT and H.E.S.S. all-electron spectrum applying the parametrization of Eq. (2) in Ohishi et al. (2021).

We followed the approach of Aleksić et al. (2012) to include the effect of the other elements. Specifically, we used helium simulations and scaled the spectrum to 0.8 of the proton spectrum to also roughly take the heavier elements into account. It should be noted, however, that helium and higher elements have very little effect on the sensitivity. As it can be seen in Fig. D.1, at high “gammaness” values, their contribution to the estimated background is smaller by about an order of magnitude than the one of protons (see also Sitarek et al. 2018). It also drops very fast with estimated energy. High rejection of proton events via the “gammaness” cut at high energies results in severely reduced background statistics. Therefore, we collected the background statistics from the inner  $1^\circ$  radius region and apply an energy-dependent correction factor between average proton density in this region and the density at camera offset of  $0.4^\circ$ . The correction factor is computed using a loose (corresponding to 94% efficiency for gamma rays) “gammaness” cut and is typically  $\sim 1.4$ .

When calculating the sensitivity using the Crab Nebula data, the background is taken around a direction in the sky with the same angular offset from the camera center as the source. For energies below 400 GeV, where the background is abundant, we used only the reflected source position to minimize systematic uncertainties, while above this value we used five background estimation regions. This approach also protects against overlapping background estimation regions at the lowest energies. Moreover, above 600 GeV, where the background is very scarce, and high angular resolution make the optimal angular distance cut from the source small, we increase the background statistics by using a broad cut for the background estimation region ( $\theta < 0.2^\circ$ ) and scale the number of events to the actual  $\theta$ -cut.

The resulting sensitivities are compared with the LST-1 standalone and MAGIC stereoscopic sensitivities in Fig. 7. The corresponding gamma-ray and background rates are presented in Fig. 8. The MAGIC-only sensitivity curve has been derived from the same dataset as used for the joint analysis. As expected, the joint analysis provides significantly better sensitivity.

Using the LST-1+MAGIC joint analysis in the medium energy range (i.e., excluding the first and last two energy bins) allows for the detection of about 30% (40%) weaker fluxes than what can be detected with MAGIC-only (LST-1-only) analysis. This is related to the addition of LST-1 rather than to the different analysis chain as the MAGIC-only performance is compatible with both chains (see Appendix C). Such a large gain in performance is expected from the stereoscopic technique when using a small number of telescopes, and this is also in line with the previous MC-based study (Di Pierro 2019), which claims a 50% improvement with respect to MAGIC. The gain is twofold: first, the addition of the third telescope improves the shower reconstruction, allowing for a more efficient rejection of the background events. Second, the number of detected gamma-ray events is also increased. Since the observations are performed in software-coincidence mode, the trigger-level collection area cannot be increased with the addition of the LST-1. However, during the regular analysis of data from MAGIC, a fraction of the images do not survive the quality cuts (small showers producing  $<50$  p.e. are typically rejected). In the MAGIC-only analysis the rejection of either M1 or M2 image is equivalent to the rejection of the whole event, since it is not possible to perform stereoscopic reconstruction with only one telescope. However the LST-1 image makes it possible to recover these kinds of events (as LST-1+M1 or LST-1+M2 event). On average, about 20% of the reconstructed gamma events has only one image from either M1 or M2 (see Table 2).

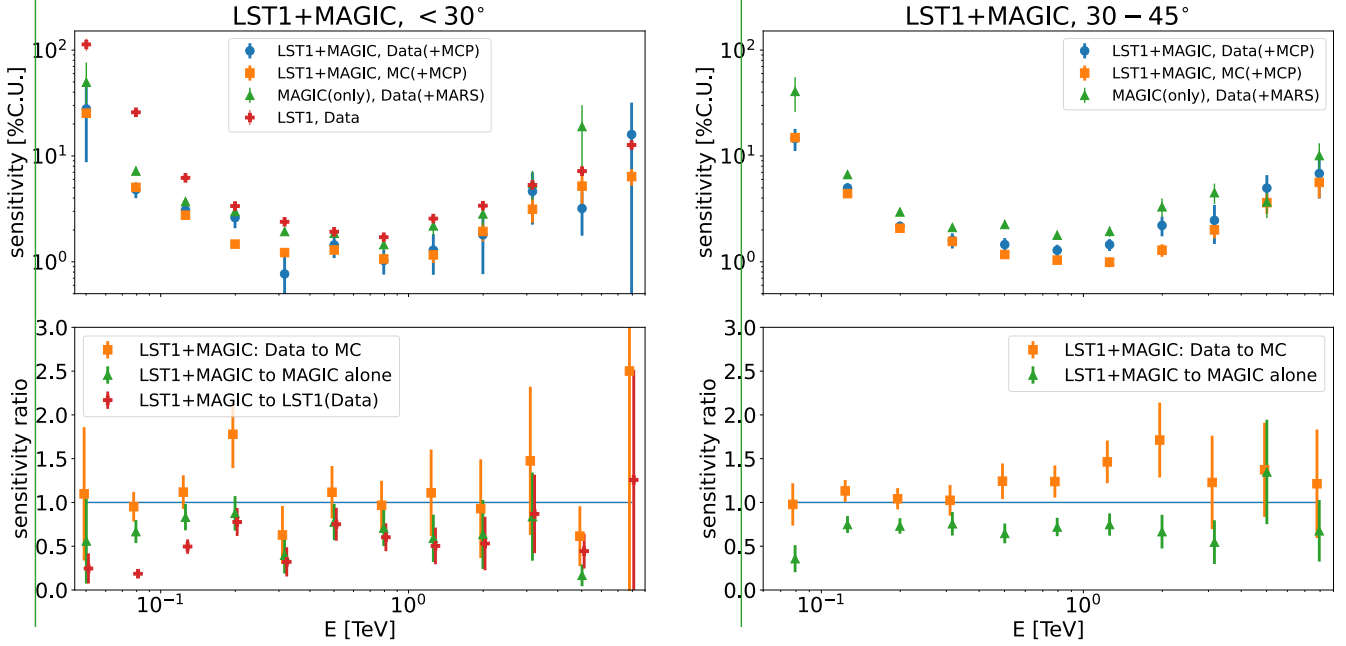


**Fig. 7.** Sensitivity in the units of Crab Nebula flux percentage of the joint LST-1+MAGIC analysis with MCP from the Crab observations (blue circles) and MC simulations (orange squares) compared to MAGIC-only analysis using MARS (green triangles) and LST-1 sensitivity (red crosses, Abe et al. 2023). Left panels: zenith distance range of  $< 30^\circ$ , while the right panels for  $30\text{--}45^\circ$ . Bottom panel: ratio of sensitivity values of the joint analysis sensitivity to MAGIC-only (green triangles) and LST-1-only (red crosses), as well as with respect to the MC sensitivity performance (orange squares); e.g., the green points shows that the three-telescope system, relative to MAGIC alone, can in average detect sources with a flux  $\sim 30\%$  lower. For visibility in the bottom panels, the points are shifted by  $\pm 2\%$  on the X scale.

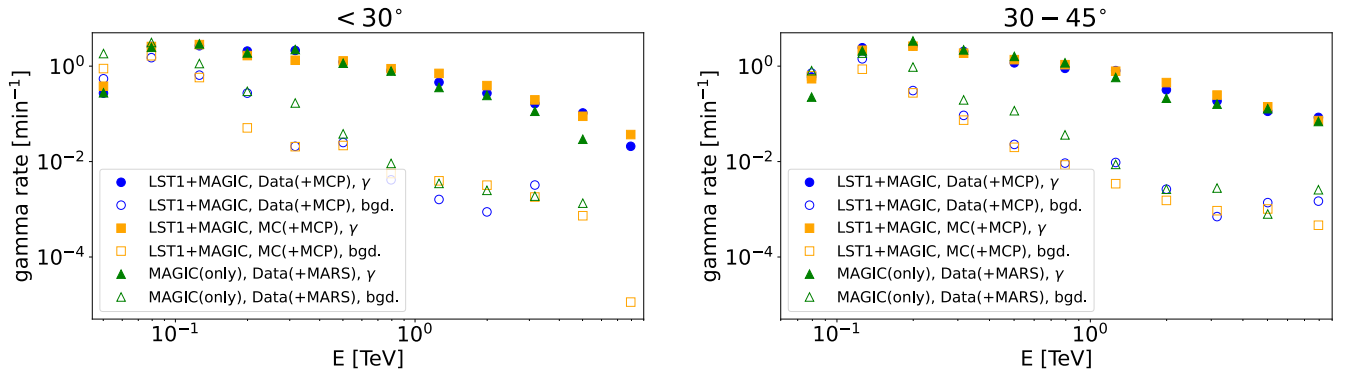


**Fig. 8.** Gamma-ray (excess, full markers) and background (empty markers) rates corresponding to the sensitivity presented in Fig. 7.

Finally, we also compared the joint analysis performance achieved with the Crab observations with the one obtained with MC simulations. In the case of low-zenith observations, the sensitivity obtained with data and MC simulations is compatible in the whole energy range. It should be noted that the data curve is based on only 0.8 hr of data (all the available Crab Nebula joint observation data taken with zenith distance below  $30^\circ$  in the data period described by the used MCs); thus, it is affected by large statistical uncertainties. In the case of medium zenith-angle observations (where also the statistical uncertainty of the sensitivity is smaller), a  $\sim 30\%$  mismatch is seen above a few hundred GeV. It might be caused by simplifications used in the MC simulations, or by an incompleteness in the background MC sample (e.g., missing events with large impact or angular offset, a simplification in the treatment higher elements, etc.). It should also be noted that a similar,  $\sim 20\%$  mismatch in sensitivity has been observed as well in the earlier simulations of the MAGIC telescopes (Aleksić et al. 2012, see also Arcaro et al. 2023).

#### 4.4. Angular resolution

To evaluate the angular resolution of the joint LST-1+MAGIC analysis in every energy bin, the gamma-ray excess was computed as a function of the angular separation to the nominal source position. To evaluate it in typical circumstances, we apply a 90% efficiency cut in “gammaness” (the same cut as used for the derivation of the spectral energy distribution of the source). We followed the commonly used definition of the angular resolution as the angular distance from the source that corresponds to 68% containment of the point spread function (see Fig. 9). To facilitate data and MC comparisons, we used reconstructed energy in both cases, assuming that at  $0.4^\circ$ , the containment is already 100% (MC simulations show that the actual containment at  $0.4^\circ$  is 96% in the lowest plotted energy bin, 63–100 GeV).

For the MAGIC-only analysis, the angular resolution is slightly higher ( $\sim 10\%$ ) in the MCP chain, as compared to the dedicated MARS analysis. It should be noted that the MARS

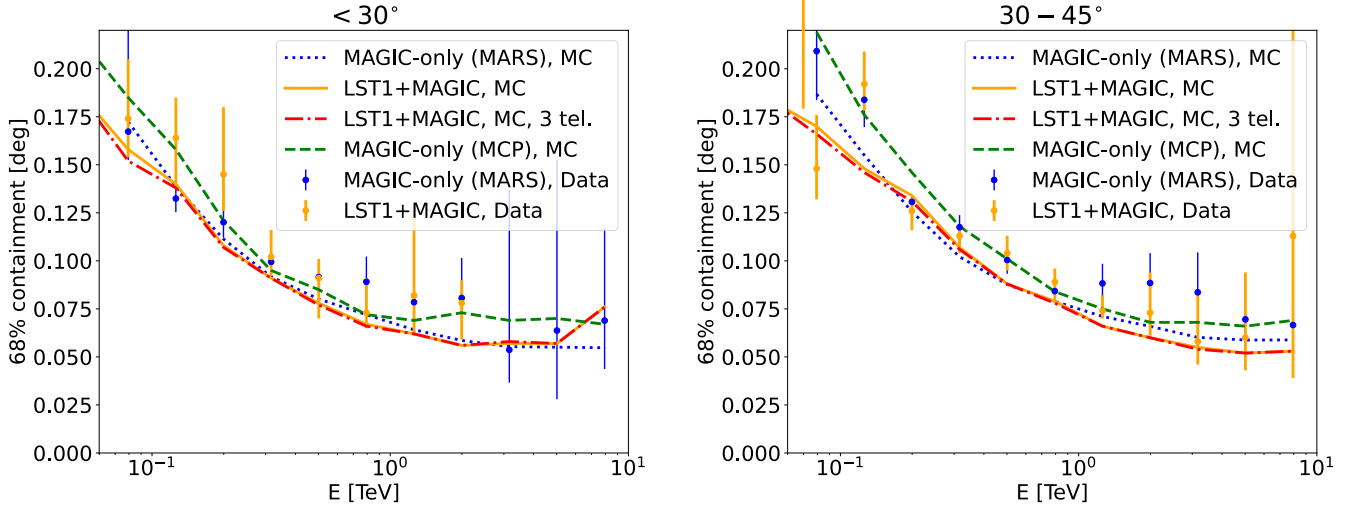


**Fig. 9.** Comparison of the angular resolution (defined as 68% containment of gamma rays) as a function of the estimated energy of the joint LST-1+MAGIC analysis (orange) from the Crab observations (points) and MC simulations (line) compared to MAGIC-only analysis using MARS (blue) or using MCP (green). Joint analysis in which only all-three telescope events are kept is shown in red (in most of the energy range the curve merges with the orange one). Left panel is for observations at low zenith angle, right panel is for the medium zenith-angle distance.

analysis software is optimized for two-telescope observations and it employs slightly different shower reconstruction techniques than `ctapipe`. As a result, at medium and high energies, the angular resolution obtained in the joint analysis with MCP is still similar to the one from MAGIC-alone observations and MARS chain. However, when comparing instead the joint analysis to MAGIC-only analysis with the same chain, a slight improvement is seen. At the lowest energies the joint analysis reaches a  $\sim 10\%$  improvement even with respect to the MARS analysis of MAGIC-only data (only visible in MC curves, as the statistics of the Crab Nebula sample are insufficient for precise evaluation in this energy range). This is likely due to the large fraction of dim images at those energies, which are better reconstructed with LST-1 than with MAGIC due to the higher light yield.

We also investigated whether further improvements can be achieved by selecting only the events in which all three images are present. A comparison of the red and orange curves in Fig. 9 indicates that such an improvement is negligible.

#### 4.5. Energy cross-calibration

The absolute energy scale calibration is one of the main problems affecting the observations with IACTs. While current IACTs claim the systematic uncertainty on the energy scale of  $\sim 15\%$  (Aleksić et al. 2016b), for the next generation LST-1 a calibration down to 4% is possible, but it requires taking into account  $\sim 20$  individual systematic effects (Gaug et al. 2019). The small distance between the LST-1 and MAGIC telescopes allows both instruments to see the same showers and to perform joint analysis, but it can also be used to compare the light yield of the telescopes (see Hofmann 2003). By selecting events seen at similar impact parameters by LST-1 and one of the MAGIC telescopes, we can compare the light yield of both instruments. In Fig. 10, we make such a comparison after applying angular and ‘‘gammaness’’ cuts to select gamma-ray events. The ratio of the total intensity of the LST-1 images to that of MAGIC-I (MAGIC-II) is 2.99 (2.60), with a standard deviation of 0.57 (0.37). This is in a rough agreement with the expectations from the larger mirror area and higher photodetector QE (see Table 1).

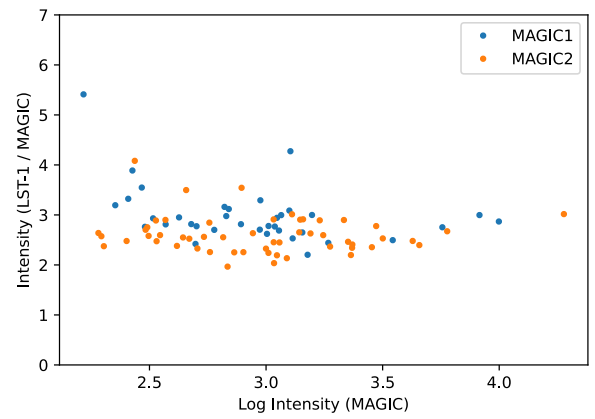


**Fig. 10.** Ratio of the reconstructed image intensities of LST-1 and MAGIC telescopes (blue: MAGIC1, orange: MAGIC2). Each point represents a single event. Only events with ‘‘gammaness’’ above 0.8 and angular distance to the Crab of below  $0.1^\circ$ , as well as the reconstructed impact parameter to both telescopes within 10 m are used. Only data with zenith distance angle below  $45^\circ$ , reconstructed impacts below 150 m and reconstructed energy above 300 GeV are used.

In order to investigate more accurately the possible relative miscalibration of the two instruments, we applied a procedure similar to that used in Aleksić et al. (2016b). Specifically, we compared the energy estimated using MAGIC camera image parameters to the one estimated for LST-1 using gamma-ray excess events. In both cases, stereoscopic parameters (impact and height of the shower maximum) were used as well. To avoid any bias present close to the energy threshold, we only used events in the estimated energy range of 0.3–3 TeV, where the energy resolution is almost constant and energy bias is negligible. We investigate the relative miscalibration of the two instruments as a function of time or zenith distance of the observations (see Fig. 11). The obtained difference in calibration of both instruments is between  $\sim 6\text{--}16\%$ , comparable to the systematic uncertainty on the energy scale of MAGIC. LST-1 estimates a higher energy than MAGIC, suggesting either an underestimation of the light collection efficiency of LST-1 in MC simulations

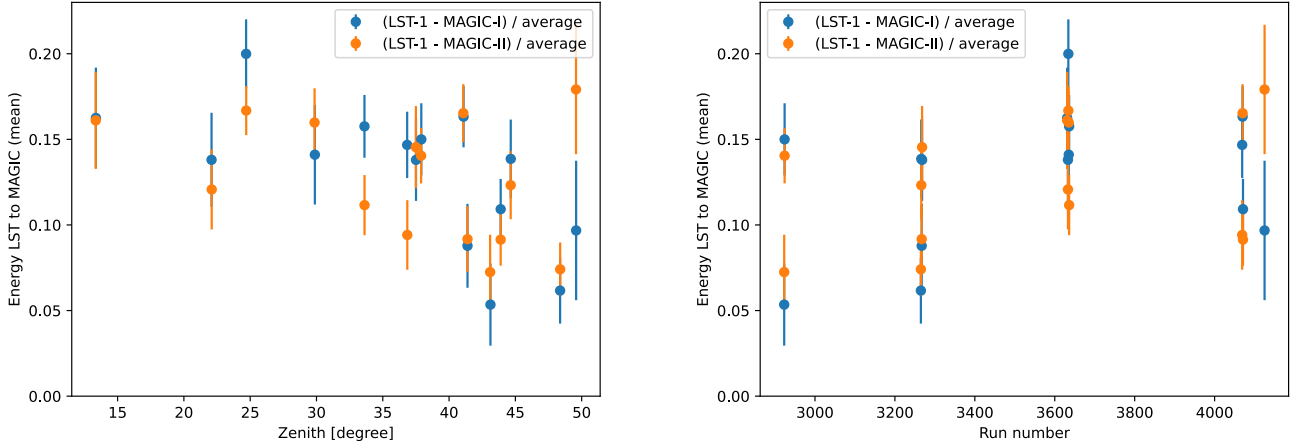


**Fig. 11.** Relative difference of estimated energy from LST-1 and MAGIC (blue for MAGIC-I, orange for MAGIC-II) camera images of the same event. The energy difference is normalized to weighted average energy obtained from all the telescopes (see Sect. 2.4). A 90% “gammaness” efficiency cut,  $0.2^\circ$  angular cut between the nominal and reconstructed source position and 0.3–3 TeV estimated energy cut are used. Each point corresponds to average from one run (with the error of the mean reported as error bar). Dependence on the zenith angle of the observation is shown in the left panel and on the LST-1 run number (increasing with time) is shown in the right panel.

or an overestimation in the case of MAGIC. No clear evolution in time is seen, but a hint of zenith dependence (with the miscalibration decreasing at medium zenith) is observed. Indeed, a constant fit to LST-1 to MAGIC-I (II) zenith dependence provides  $\chi^2/N_{\text{dof}} = 48.8/14$  ( $\chi^2/N_{\text{dof}} = 49.5/14$ ), while a simple linear fit improves the  $\chi^2/N_{\text{dof}}$  values to 27.7/13 (33.0/13).

#### 4.6. Energy resolution

In the absence of an external calibrator, the energy resolution of an IACT can only be derived using MC simulations. To evaluate the performance of the energy reconstruction, we divided the data into bins of true energy,  $E_{\text{true}}$ , and in each bin, we determined the distribution of the energy dispersion,  $(E_{\text{est}} - E_{\text{true}})/E_{\text{true}}$ . We defined the energy bias as the median of this distribution (while confirming that using the mean instead would not affect the estimation considerably). Similarly to the angular resolution, we define the energy resolution as the 68% containment area of the dispersion. We first compute the difference between the median of the distribution and the 16% and 84% quantiles, which correspond to the underestimation and overestimation of the energy estimation. Next, we computed the 68% quantile energy resolution as the average (weighted with inversed variance) of these underestimation and overestimation components. For comparison we also computed the energy resolution as the standard deviation of a Gaussian fit to the  $(E_{\text{est}} - E_{\text{true}})/E_{\text{true}}$  distribution excluding the tails. The results are shown in Fig. 12 and summarized in Table E.3.

The energy estimation has nearly no bias down to  $\sim 150$  GeV. At the lowest energies, the energy resolution is improved with respect to MAGIC-alone observations (cf. Ishio & Paneque 2022). The energy resolution in the medium energy range is  $\sim 14\%$ . At multi-TeV energies, the energy resolution starts to worsen. The 68% containment definition provides very similar results as a narrow fit definition. As the standard deviation is increased by outliers, this definition reports worse energy estimation, in particular at the highest energies. It should be noted that most of the events above a few TeV in the joint analysis are not fully contained in the camera (i.e., they have pixels surviving the image cleaning in the outermost ring of the camera). We also note that the performance of the energy estimation

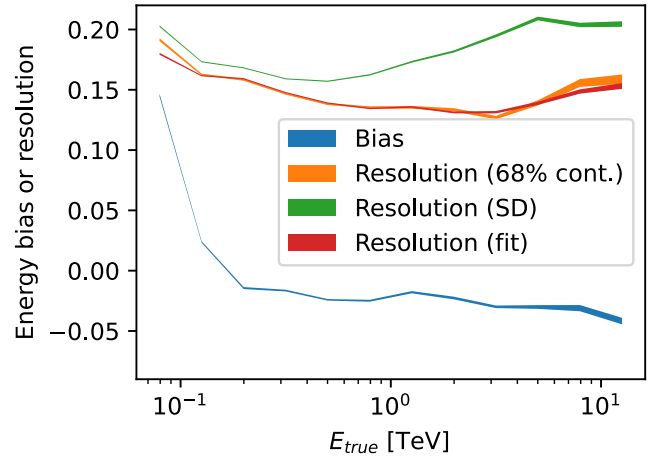


**Fig. 12.** Energy resolution obtained with MC simulations for gamma-ray showers at zenith angle distance of  $23.6^\circ$ . The resolution is calculated as an average 68% quantile (orange). Standard deviation of the energy misreconstruction is shown in green. The red line is the resolution value obtained from a tail-less (performed in the range  $\text{mean} \pm 2$  standard deviations) Gaussian fit. The bias of the energy estimation ( $(E_{\text{est}} - E_{\text{true}})/E_{\text{true}}$ ) is shown in blue. The thickness of the lines represents the statistical uncertainty. A “gammaness” efficiency cut of 90%, angular distance of  $<0.2^\circ$  and “intensity” of  $>50$  p.e. cuts are applied.

at the highest energies is strongly affected by the details of the training. In particular, it varies whether the training is done on diffuse gamma rays or with gamma rays produced in a ring with radius equal to the expected offset used during observations of point-like sources. It also depends on the event statistics used in the training.

In order to validate the accuracy of the claimed energy estimation, we performed a similar test as the one described in Aleksić et al. (2016b; see also Fig. 11), comparing the spread of the energy estimation between the telescopes. Contrary to the energy resolution, such a spread can be then compared with the one obtained from the MC simulations. As can be seen in Fig. 13 the inter-telescope spread of the energy estimation is relatively well reproduced for all the zenith angles, further supporting the reported energy resolution values.

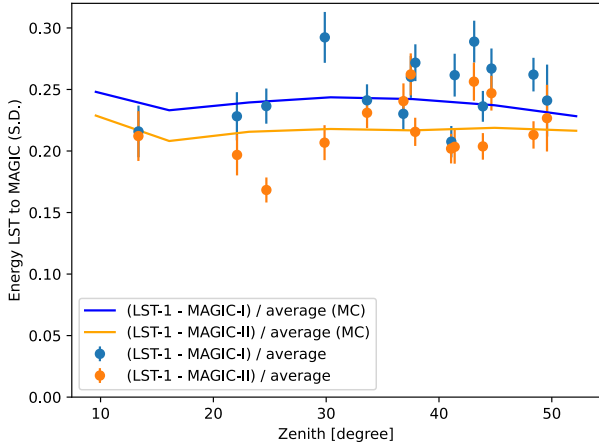


**Fig. 13.** Standard deviation of the relative difference in estimated energy between one of the MAGIC telescopes and LST-1 for the same event. Data, MC, and quality selection cuts as in Fig. 11

#### 4.7. Comparison to single instrument analysis

The systematic errors affecting measurements performed with IACTs stem both from the complex hardware and from the imperfect knowledge of the atmosphere status, which is considered as part of the detector. The systematic uncertainties of MAGIC are divided into three categories: uncertainty of the energy scale of 15%, pure flux normalization uncertainty of 11–18% and uncertainty of the spectral slope of  $\pm 0.15$  for an assumed power-law spectrum (Aleksić et al. 2016b). In the case of LST-1 standalone observations, the uncertainty of the background estimation plays an important role at the lowest energies (Abe et al. 2023) because single-telescope observations are characterized by much higher background rates (note: no detailed study of the systematic uncertainties of LST-1 has been performed yet).

In the joint analysis, we combined the data from two different IACT systems. Such a combination might on one hand increase the systematic uncertainties, in particular, due to simplifications needed to merge the simulation and analysis chains for both instruments. On the other hand the resulting systematic uncertainties might also decrease because of averaging. Moreover, the atmospheric transmission is one of the main sources of systematic uncertainty for IACTs (Aleksić et al. 2012) and it can also vary on different time scales. Due to the physical proximity of MAGIC and LST-1, both instruments share the same contribution from the atmospheric transmission uncertainty.

While some energy miscalibration between LST-1 and MAGIC has been observed, it is within the claimed systematic uncertainties of MAGIC. Moreover, the fact that the reconstructed spectrum agrees closely (within  $\sim 10\%$ ) with the MAGIC and LST-1 standalone results further supports that the systematic uncertainties of the joint analysis are not larger than those of individual instruments. The light curve stability analysis requires 12.7% (7.9%) relative systematic uncertainties to be consistent with a constant flux on run (day) timescales. Those numbers are remarkably similar to those obtained from such a study for MAGIC-only data: 11% on run-by-run (Aleksić et al. 2016b) and 7.6% on day-to-day (Ahnen et al. 2017). In the case of LST-1-alone observations, the required variable systematic uncertainties on day-to-day time scale are even slightly lower: 6–7% (Abe et al. 2023); however, that study was limited only to low zenith distance observations. Therefore, we conclude that

the systematic uncertainties of the joint analysis are similar to those of MAGIC.

## 5. Conclusions

In this work, we introduce a new pipeline enabling the joint analysis of LST-1 and MAGIC data. The LST Collaboration is aimed at performing 50% of the observations together with MAGIC in the coming years. The chain provides common stereoscopic analysis of images corresponding to the same physical shower. This study is also a path-finder for a stereoscopic analysis chain to be applied to the future CTAO arrays. As the events are matched by arrival time from the individual LST-1 and MAGIC observations, the rate of events cannot be increased at the trigger level. However, the addition of the LST-1 allows us to reconstruct 20% more events in which one of the MAGIC images is rejected during reconstruction – and, thus, where no stereoscopic analysis is possible with MAGIC only. The analysis provides an improvement of the energy threshold at the reconstruction level by  $\sim 15\%$  with respect to MAGIC-only observations. As a result of such recovered events, and of the improved background rejection for events seen by all three telescopes, the performance of joint observations is greatly improved. In particular, the minimum detectable flux is 30% (40%) lower than MAGIC-alone (LST-1-alone) analysis. Since in the medium energy range the sensitivity is inversely proportional to the square root of observation time, this corresponds to 2-fold (nearly 3-fold) shortening of the required observation time to reach the same performance of MAGIC-only (LST-1-only) observations. Therefore the two systems work more efficiently together than individually and joint observations are highly valued.

The other performance parameters, in particular, the angular and energy resolution are not strongly affected by the addition of the LST-1 telescope, only minor improvements are seen at the lowest energies. The presented analysis is designed to improve the collection area of MAGIC-alone observations by allowing for the inclusion for events that would not survive the standard analysis chain of MARS due to one of the images not surviving the quality cuts. The additional reconstruction of these kinds of worse-quality events partially contributes to this lack of significant improvement. It is also possible that the peculiar geometrical placement of the three telescopes (obtuse-angled triangle) worsens the efficiency of the shower reconstruction. Moreover the comparisons are performed with the MARS analysis of MAGIC data, optimized for the two-telescope case, and cannot be fully scaled to multiple telescopes. Further optimization of the analysis for improved angular or energy resolution is possible, possibly at the price of decreased collection area.

We performed comparison checks, both against the MAGIC standard simulation software as well as comparisons of the simulation results to the data and showed a rather good agreement. The Crab Nebula spectrum obtained from the joint analysis can be described as  $dN/dE = (3.48 \pm 0.09_{\text{stat}}) \times 10^{-11} (E/1\text{TeV})^{-2.49 \pm 0.03_{\text{stat}} - (0.117 \pm 0.017_{\text{stat}}) \ln(E/1\text{TeV})} \text{ cm}^{-2} \text{ s}^{-1} \text{ TeV}^{-1}$ . It is within about 10% of the earlier measurements. Also, the derived flux stability is comparable to the one of MAGIC, pointing to similar systematic uncertainty of the joint analysis.

*Acknowledgements.* We gratefully acknowledge financial support from the following agencies and organisations: Ministry of Education, Youth and Sports, MEYS LM2015046, LM2018105, LTT17006, EU/MEYS CZ.02.1.01/0.0/0.0/16\_013/0001403, CZ.02.1.01/0.0/0.0/18\_046/0016007 and CZ.02.1.01/0.0/0.0/16\_019/0000754, Czech Republic; Max Planck Society, German Bundesministerium für Bildung und Forschung (Verbundforschung/ErUM), Deutsche Forschungsgemeinschaft (SFBs 876 and 1491), Germany;

Istituto Nazionale di Astrofisica (INAF), Istituto Nazionale di Fisica Nucleare (INFN), Italian Ministry for University and Research (MUR); ICRR, University of Tokyo, JSPS, MEXT, Japan; JST SPRING – JPMJSP2108; Narodowe Centrum Nauki, grant number 2019/34/E/ST9/00224, Poland; The Spanish groups acknowledge the Spanish Ministry of Science and Innovation and the Spanish Research State Agency (AEI) through the government budget lines PGE2021/28.06.000X.411.01, PGE2022/28.06.000X.411.01 and PGE2022/28.06.000X.711.04, and grants PGC2018-095512-B-I00, PID2019-104114RB-C31, PID2019-107847RB-C44, PID2019-104114RB-C32, PID2019-105510GB-C31, PID2019-104114RB-C33, PID2019-107847RB-C41, PID2019-107847RB-C43, PID2019-107988GB-C22; the “Centro de Excelencia Severo Ochoa” program through grants no. CEX2021-001131-S, CEX2019-000920-S; the “Unidad de Excelencia María de Maeztu” program through grants no. CEX2019-000918-M, CEX2020-001058-M; the “Juan de la Cierva-Incorporación” program through grant no. IJC2019-040315-I. They also acknowledge the “Programa Operativo” FEDER 2014-2020, Consejería de Economía y Conocimiento de la Junta de Andalucía (Ref. 1257737), PAIDI 2020 (Ref. P18-FR-1580) and Universidad de Jaén; “Programa Operativo de Crecimiento Inteligente” FEDER 2014-2020 (Ref. ESFRI-2017-IAC-12), Ministerio de Ciencia e Innovación, 15% co-financed by Consejería de Economía, Industria, Comercio y Conocimiento del Gobierno de Canarias; the “CERCA” program of the Generalitat de Catalunya; and the European Union’s “Horizon 2020” GA:824064 and NextGenerationEU; We acknowledge the Ramon y Cajal program through grant RYC-2020-028639-I and RYC-2017-22665; State Secretariat for Education, Research and Innovation (SERI) and Swiss National Science Foundation (SNSF), Switzerland; The research leading to these results has received funding from the European Union’s Seventh Framework Programme (FP7/2007-2013) under grant agreements No 262053 and No 317446. This project is receiving funding from the European Union’s Horizon 2020 research and innovation programs under agreement No 676134. ESCAPE – The European Science Cluster of Astronomy & Particle Physics ESFRI Research Infrastructures has received funding from the European Union’s Horizon 2020 research and innovation programme under Grant Agreement no. 824064. We would like to thank the Instituto de Astrofísica de Canarias for the excellent working conditions at the Observatorio del Roque de los Muchachos in La Palma. The financial support of the German BMBF, MPG and HGF; the Italian INFN and INAF; the Swiss National Fund SNF; the grants PID2019-104114RB-C31, PID2019-104114RB-C32, PID2019-104114RB-C33, PID2019-105510GB-C31, PID2019-107847RB-C41, PID2019-107847RB-C42, PID2019-107847RB-C44, PID2019-107988GB-C22 funded by the Spanish MCIN/AEI/ 10.13039/501100011033; the Indian Department of Atomic Energy; the Japanese ICRR, the University of Tokyo, JSPS, and MEXT; the Bulgarian Ministry of Education and Science, National RI Roadmap Project DOI-400/18.12.2020 and the Academy of Finland grant nr. 320045 is gratefully acknowledged. This work was also been supported by Centros de Excelencia “Severo Ochoa” y Unidades “María de Maeztu” program of the Spanish MCIN/AEI/10.13039/501100011033 (SEV-2016-0588, CEX2019-000920-S, CEX2019-000918-M, CEX2021-001131-S, MDM-2015-0509-18-2) and by the CERCA institution of the Generalitat de Catalunya; by the Croatian Science Foundation (HrZZ) Project IP-2016-06-9782 and the University of Rijeka Project uniri-prirod-18-48; by the Deutsche Forschungsgemeinschaft (SFB1491 and SFB876); the Polish Ministry Of Education and Science grant No. 2021/WK/08; and by the Brazilian MCTIC, CNPq and FAPERJ. This work was conducted in the context of the CTA LST Project. A. Berti: development and maintenance of the module `ctapipe_io_magic`, implementation of processing of MAGIC calibrated data within `magic-cta-pipe`, general maintenance of the `magic-cta-pipe` package; F. Di Pierro: development of the simultaneous observations’ database and of the first versions of `ctapipe_io_magic`, cross-checks with the MARS analysis, coordination of the analysis cross-checks; E. Jobst: implementation of tests for low-level comparison of shower images and parameters for MAGIC-only analysis, upgrade of `ctapipe_io_magic` to new releases of `ctapipe`, test of `magic-cta-pipe` for MAGIC-only analysis; Y. Ohtani: responsible for most of `magic-cta-pipe` analysis code, many tests and optimization of the pipeline, calculation of performance parameters; J. Sitarek: reoptimization and processing of Monte Carlo simulations, calculation of performance parameters, paper drafting; Y. Suda: contribution to the first iteration of implementation of MAGIC to `sim_telarray` and coordinating the group from the MAGIC side together with F. Di Pierro; E. Visentin: performance parameters cross-check analysis. The rest of the authors have contributed in one or several of the following ways: design, construction, maintenance and operation of the instrument(s); preparation and/or evaluation of the observation proposals; data acquisition, processing, calibration and/or reduction; production of analysis tools and/or related Monte Carlo simulations; discussion and approval of the contents of the draft. J.S. would like to thank ICRR for excellent working conditions during final stages of preparation of this manuscript. Y.S.’ work was supported by JSPS KAKENHI Grant Number JP21K20368 and JP23K13127. The authors would like to thank anonymous journal referee for the feedback which helped to improve the paper.

## References

- Abe, S., Abe, H., Abe, K., et al. 2023, *ApJ*, **956**, 80
- Acharya, B., Actis, M., Aghajani, T., et al. 2013 *Astropart. Phys.*, **43**, 3
- Aharonian, F., Akhperjanian, A. G., Bazer-Bachi, A. R., et al. 2006, *A&A*, **457**, 899
- Ahnen, M. L., Ansoldi, S., Antonelli, L. A., et al. 2017, *Astropart. Phys.*, **94**, 29
- Aleksić, J., Antonelli, L. A., Antoranz, P., et al. 2010, *A&A*, **524**, A77
- Aleksić, J., Alvarez, E. A., Antonelli, L. A., et al. 2012, *Astropart. Phys.*, **35**, 435
- Aleksić, J., Ansoldi, S., Antonelli, L. A., et al. 2015, *J. High Energy Astrophys.*, **5**, 30
- Aleksić, J., Ansoldi, S., Antonelli, L. A., et al. 2016a, *Astropart. Phys.*, **72**, 61
- Aleksić, J., Ansoldi, S., Antonelli, L. A., et al. 2016b, *Astropart. Phys.*, **72**, 76
- Arcaro, C., Doro, M., Sitarek, J., et al. 2023, *Astropart. Phys.*, **155**, 102902
- Bernlöhr, K. 2008, *Astropart. Phys.*, **30**, 149
- Breiman, L. 2001, *Mach. Learn.*, **45**, 5
- CTA-LST Project 2021, *J. Phys. Conf. Ser.*, **2156**, 012089
- CTA-LST Project (Abe, H., et al.) 2022, *Int. Cosmic Ray Conf.*, **37**, 872
- Deil, C., Zanin, R., Lefaucheur, J., et al. 2017, *Int. Cosmic Ray Conf.*, **35**, 766
- Di Pierro, F. 2019, *Int. Cosmic Ray Conf.*, **36**, 659
- Donath, A., Deil, Ch., Terrier, R., et al., 2022, <https://zenodo.org/records/6552377>
- Gaug, M., Fegan, S., Mitchell, A. M. W., et al. 2019, *APJS*, **243**, 11
- Heck, D., Knapp, J., Capdevielle, J. N., Schatz, G., & Thouw, T. 1998, *CORSIKA: a Monte Carlo code to simulate extensive air showers*
- H.E.S.S. Collaboration 2006, *Nucl. Phys. B Proc. Suppl.*, **151**, 373
- Hillas, A. M. 1985, *Int. Cosmic Ray Conf.*, **3**, 445
- Hofmann, W. 2003, *Astropart. Phys.*, **20**, 1
- Hofmann, W., Jung, I., Konopelko, A., et al. 1999, *Astropart. Phys.*, **12**, 135
- Holler, M., Berge, D., van Eldik, C., et al. 2015, ArXiv e-prints [arXiv:1509.02902]
- Ishio, K., & Paneque, D. 2022, arXiv e-prints [arXiv:2212.03592]
- Kohnle, A., Aharonian, F., Akhperjanian, A., et al. 1996, *Astropart. Phys.*, **5**, 119
- Kosack, K., Nothe, M., Watson, J., et al. 2022, <https://zenodo.org/records/8335474>
- Lessard, R. W., Buckley, J. H., Connaughton, V., et al. 2001, *Astropart. Phys.*, **15**, 1
- Li, T.-P., & Ma, Y.-Q. 1983, *ApJ*, **272**, 317
- Lopez-Coto, R., Vuillaume, T., Moralejo, A., et al. 2022, <https://zenodo.org/records/8377093>
- Lyard, E., Walter, R., & Consortium, C. 2017, *Int. Cosmic Ray Conf.*, **301**, 843
- Majumdar, P., Moralejo, A., Bigongiari, C., et al. 2005, *Int. Cosmic Ray Conf.*, **5**, 203
- Meyer, M., Horns, D., & Zechlin, H.-S. 2010, *A&A*, **523**, A2
- Moralejo, A., Gaug, M., Carmona, E., et al. 2009, ArXiv e-prints [arXiv:0907.0943]
- Mosteller F., & Tukey J. W. 1968, *Data analysis, including statistics. In Handbook of Social Psychology* (Reading, MA: Addison-Wesley)
- Nigro, C., Deil, C., Zanin, R., et al. 2019, *A&A*, **625**, A10
- Nothe, M., Kosack, K., Nickel, L., et al. 2022, *Int. Cosmic Ray Conf.*, **395**, 744
- Nozaki, S., Awai, K., Bamba, A., et al. 2020, *Proc. SPIE*, **11447**, 11447
- Ohishi, M., Arbeletche, L., de Souza, V., et al. 2021, *J. Phys. G Nucl. Phys.*, **48**, 075201
- Pedregosa, F., Varoquaux, G., Gramfort, A., et al. 2011, *J. Mach. Learn. Res.*, **12**, 2825
- Pence, W., Seaman, R., & White, R. L. 2012, arXiv e-prints [arXiv:1201.1340]
- Sitarek, J. 2022, *Galaxies*, **10**, 21
- Sitarek, J., Gaug, M., Mazin, D., et al. 2013, *Nucl. Instrum. Methods Phys. Res. A*, **723**, 109
- Sitarek, J., Sobczyńska, D., Szanecki, M., et al. 2018, *Astropart. Phys.*, **97**, 1
- Yue, C., De Benedittis, A., Mazziotta, M. N., et al. 2019, *Int. Cosmic Ray Conf.*, **36**, 163
- Zanin R., Carmona, E., Sitarek, J., et al. 2013, *Proc. ICRC 2013*, 773

- <sup>1</sup> Institute for Cosmic Ray Research, University of Tokyo, 5-1-5 Kashiwa-no-ha, Kashiwa, Chiba 277-8582, Japan
- <sup>2</sup> Department of Physics, Tokai University, 4-1-1 Kita-Kaname, Hiratsuka, Kanagawa 259-1292, Japan
- <sup>3</sup> Instituto de Astrofísica de Canarias and Departamento de Astrofísica, Universidad de La Laguna, La Laguna, Tenerife, Spain
- <sup>4</sup> Departament de Física Quàntica i Astrofísica, Institut de Ciències del Cosmos, Universitat de Barcelona, IEEC-UB, Martí i Franquès 1, 08028 Barcelona, Spain
- <sup>5</sup> Instituto de Astrofísica de Andalucía-CSIC, Glorieta de la Astronomía s/n, 18008 Granada, Spain

- <sup>6</sup> Grupo de Electronica, Universidad Complutense de Madrid, Av. Complutense s/n, 28040 Madrid, Spain
- <sup>7</sup> National Institute for Astrophysics (INAF), 00136 Rome, Italy
- <sup>8</sup> INFN Sezione di Trieste and Università degli studi di Udine, via delle scienze 206, 33100 Udine, Italy
- <sup>9</sup> International Center for Relativistic Astrophysics (ICRA), Rome, Italy
- <sup>10</sup> INAF – Osservatorio Astronomico di Roma, Via di Frascati 33, 00040, Monteporzio Catone, Italy
- <sup>11</sup> INFN Sezione di Napoli, Via Cintia, ed. G, 80126 Napoli, Italy
- <sup>12</sup> Max-Planck-Institut für Physik, Föhringer Ring 6, 80805 München, Germany
- <sup>13</sup> Università di Padova and INFN, 35131 Padova, Italy
- <sup>14</sup> Institut de Física d'Altes Energies (IFAE), The Barcelona Institute of Science and Technology, Campus UAB, 08193 Bellaterra (Barcelona), Spain
- <sup>15</sup> Univ. Savoie Mont Blanc, CNRS, Laboratoire d'Annecy de Physique des Particules – IN2P3, 74000 Annecy, France
- <sup>16</sup> Department of Physics, TU Dortmund University, Otto-Hahn-Str. 4, 44227 Dortmund, Germany
- <sup>17</sup> Croatian MAGIC Group, University of Zagreb, Faculty of Electrical Engineering and Computing (FER), 10000 Zagreb, Croatia
- <sup>18</sup> Universität Hamburg, Institut für Experimentalphysik, Luruper Chaussee 149, 22761 Hamburg, Germany
- <sup>19</sup> Graduate School of Science, University of Tokyo, 7-3-1 Hongo, Bunkyo-ku, Tokyo 113-0033, Japan
- <sup>20</sup> IPARCOS-UCM, Instituto de Física de Partículas y del Cosmos, and EMFTEL Department, Universidad Complutense de Madrid, 28040 Madrid, Spain
- <sup>21</sup> Faculty of Science and Technology, Universidad del Azuay, Cuenca, Ecuador
- <sup>22</sup> INAF – Osservatorio di Astrofisica e Scienza dello spazio di Bologna, Via Piero Gobetti 93/3, 40129 Bologna, Italy
- <sup>23</sup> Centro Brasileiro de Pesquisas Físicas, Rua Xavier Sigaud 150, RJ 22290-180, Rio de Janeiro, Brazil
- <sup>24</sup> INFN Sezione di Padova and Università degli Studi di Padova, Via Marzolo 8, 35131 Padova, Italy
- <sup>25</sup> Faculty of Physics and Applied Informatics, University of Lodz, ul. Pomorska 149-153, 90-236 Lodz, Poland
- <sup>26</sup> Centro de Investigaciones Energéticas, Medioambientales y Tecnológicas, 28040 Madrid, Spain
- <sup>27</sup> ETH Zürich, CH-8093 Zürich, Switzerland
- <sup>28</sup> INFN Sezione di Bari and Politecnico di Bari, via Orabona 4, 70124 Bari, Italy
- <sup>29</sup> INAF – Osservatorio Astronomico di Brera, Via Brera 28, 20121 Milano, Italy
- <sup>30</sup> University of Geneva, Département de physique nucléaire et corpusculaire, 24 Quai Ernest Ansermet, 1211 Genève 4, Switzerland
- <sup>31</sup> INFN Sezione di Catania, Via S. Sofia 64, 95123 Catania, Italy
- <sup>32</sup> Departament de Física, and CERES-IEEC, Universitat Autònoma de Barcelona, 08193 Bellaterra, Spain
- <sup>33</sup> INAF – Istituto di Astrofisica e Planetologia Spaziali (IAPS), Via del Fosso del Cavaliere 100, 00133 Roma, Italy
- <sup>34</sup> Università di Pisa and INFN Pisa, 56126 Pisa, Italy
- <sup>35</sup> Aix-Marseille Univ., CNRS/IN2P3, CPPM, Marseille, France
- <sup>36</sup> INFN Sezione di Bari and Università di Bari, via Orabona 4, 70126 Bari, Italy
- <sup>37</sup> INFN Sezione di Torino, Via P. Giuria 1, 10125 Torino, Italy
- <sup>38</sup> Palacky University Olomouc, Faculty of Science, 17 listopadu 1192/12, 771 46 Olomouc, Czech Republic
- <sup>39</sup> Department for Physics and Technology, University of Bergen, Norway
- <sup>40</sup> Institute for Astro- and Particle Physics, University of Innsbruck, 6020 Innsbruck, Austria
- <sup>41</sup> University of Alcalá UAH, Departamento de Physics and Mathematics, Pza. San Diego, 28801, Alcalá de Henares, Madrid, Spain
- <sup>42</sup> INFN MAGIC Group, INFN Sezione di Catania and Dipartimento di Fisica e Astronomia, University of Catania, 95123 Catania, Italy
- <sup>43</sup> Port d'Informació Científica (PIC), 08193 Bellaterra (Barcelona), Spain
- <sup>44</sup> Port d'Informació Científica, Edifici D, Carrer de l'Albareda, 08193 Bellaterra (Cerdanyola del Vallès), Spain
- <sup>45</sup> INFN MAGIC Group, INFN Sezione di Torino and Università degli Studi di Torino, 10125 Torino, Italy
- <sup>46</sup> University of Rijeka, Department of Physics, Radmile Matejčić 2, 51000 Rijeka, Croatia
- <sup>47</sup> Institute for Theoretical Physics and Astrophysics, Universität Würzburg, Campus Hubland Nord, Emil-Fischer-Str. 31, 97074 Würzburg, Germany
- <sup>48</sup> Institut für Theoretische Physik, Lehrstuhl IV: Plasma-Astroteilchenphysik, Ruhr-Universität Bochum, Universitätsstraße 150, 44801 Bochum, Germany
- <sup>49</sup> INFN Sezione di Roma La Sapienza, P.le Aldo Moro 2, 00185 Rome, Italy
- <sup>50</sup> ILANCE, CNRS – University of Tokyo International Research Laboratory, Kashiwa, Chiba 277-8582, Japan
- <sup>51</sup> Physics Program, Graduate School of Advanced Science and Engineering, Hiroshima University, 739-8526 Hiroshima, Japan
- <sup>52</sup> Deutsches Elektronen-Synchrotron (DESY), 15738 Zeuthen, Germany
- <sup>53</sup> INFN Sezione di Roma Tor Vergata, Via della Ricerca Scientifica 1, 00133 Rome, Italy
- <sup>54</sup> Armenian MAGIC Group: ICRANet-Armenia, 0019 Yerevan, Armenia
- <sup>55</sup> University of Split, FESB, R. Boškovića 32, 21000 Split, Croatia
- <sup>56</sup> Department of Physics, Yamagata University, Yamagata, Yamagata 990-8560, Japan
- <sup>57</sup> Josip Juraj Strossmayer University of Osijek, Department of Physics, Trg Ljudevita Gaja 6, 31000 Osijek, Croatia
- <sup>58</sup> INFN Dipartimento di Scienze Fisiche e Chimiche – Università degli Studi dell'Aquila and Gran Sasso Science Institute, Via Vetoio 1, Viale Crispi 7, 67100 L'Aquila, Italy
- <sup>59</sup> Kitashirakawa Oiwakecho, Sakyo Ward, Kyoto, 606-8502, Japan
- <sup>60</sup> Finnish MAGIC Group, Finnish Centre for Astronomy with ESO, University of Turku, 20014 Turku, Finland
- <sup>61</sup> FZU – Institute of Physics of the Czech Academy of Sciences, Na Slovance 1999/2, 182 21 Praha 8, Czech Republic
- <sup>62</sup> Astronomical Institute of the Czech Academy of Sciences, Bocni II 1401, 14100 Prague, Czech Republic
- <sup>63</sup> Faculty of Science, Ibaraki University, Mito, Ibaraki 310-8512, Japan
- <sup>64</sup> Faculty of Science and Engineering, Waseda University, Shinjuku, Tokyo 169-8555, Japan
- <sup>65</sup> Department of Physics, University of Oslo, Norway
- <sup>66</sup> Institute of Particle and Nuclear Studies, KEK (High Energy Accelerator Research Organization), 1-1 Oho, Tsukuba 305-0801, Japan
- <sup>67</sup> INFN Sezione di Trieste and Università degli Studi di Trieste, Via Valerio 2 I, 34127 Trieste, Italy
- <sup>68</sup> INFN and Università degli Studi di Siena, Dipartimento di Scienze Fisiche, della Terra e dell'Ambiente (DSFTA), Sezione di Fisica, Via Roma 56, 53100 Siena, Italy
- <sup>69</sup> Escuela Politécnica Superior de Jaén, Universidad de Jaén, Campus Las Lagunillas s/n, Edif. A3, 23071 Jaén, Spain
- <sup>70</sup> Department of Astronomy, University of Geneva, Chemin d'Ecogia 16, 1290 Versoix, Switzerland
- <sup>71</sup> Saha Institute of Nuclear Physics, Bidhannagar, Kolkata-700 064, India
- <sup>72</sup> Institute for Nuclear Research and Nuclear Energy, Bulgarian Academy of Sciences, 72 boul. Tsarigradsko chaussee, 1784 Sofia, Bulgaria
- <sup>73</sup> Dipartimento di Fisica e Chimica 'E. Segrè', Università degli Studi di Palermo, via delle Scienze, 90128 Palermo
- <sup>74</sup> Università di Siena and INFN Pisa, 53100 Siena, Italy
- <sup>75</sup> Hiroshima Astrophysical Science Center, Hiroshima University, Higashi-Hiroshima, Hiroshima 739-8526, Japan
- <sup>76</sup> School of Allied Health Sciences, Kitasato University, Sagamihara, Kanagawa 228-8555, Japan

- <sup>77</sup> RIKEN, Institute of Physical and Chemical Research, 2-1 Hirosawa, Wako, Saitama, 351-0198, Japan
- <sup>78</sup> Laboratory for High Energy Physics, École Polytechnique Fédérale, 1015 Lausanne, Switzerland
- <sup>79</sup> Finnish MAGIC Group, Space Physics and Astronomy Research Unit, University of Oulu, 90014 Oulu, Finland
- <sup>80</sup> Charles University, Institute of Particle and Nuclear Physics, V Holešovičkách 2, 180 00 Prague 8, Czech Republic
- <sup>81</sup> Division of Physics and Astronomy, Graduate School of Science, Kyoto University, Sakyo-ku, Kyoto 606-8502, Japan
- <sup>82</sup> Institute for Space-Earth Environmental Research, Nagoya University, Chikusa-ku, Nagoya 464-8601, Japan
- <sup>83</sup> Kobayashi-Maskawa Institute (KMI) for the Origin of Particles and the Universe, Nagoya University, Chikusa-ku, Nagoya 464-8602, Japan
- <sup>84</sup> Graduate School of Technology, Industrial and Social Sciences, Tokushima University, Tokushima 770-8506, Japan
- <sup>85</sup> INAF – Osservatorio astronomico di Padova, Vicolo Osservatorio 5, 35122 Padova, Italy
- <sup>86</sup> Department of Physical Sciences, Aoyama Gakuin University, Fuchinobe, Sagami-hara, Kanagawa, 252-5258, Japan
- <sup>87</sup> IRFU, CEA, Université Paris-Saclay, Bât. 141, 91191 Gif-sur-Yvette, France
- <sup>88</sup> Graduate School of Science and Engineering, Saitama University, 255 Simo-Ohkubo, Sakura-ku, Saitama city, Saitama 338-8570, Japan
- <sup>89</sup> Institute of Space Sciences (ICE, CSIC), and Institut d'Estudis Espacials de Catalunya (IEEC), and Institució Catalana de Recerca I Estudis Avançats (ICREA), Campus UAB, Carrer de Can Magrans, s/n 08193 Bellaterra, Spain
- <sup>90</sup> INFN MAGIC Group, INFN Sezione di Perugia, 06123 Perugia, Italy
- <sup>91</sup> Dipartimento di Fisica – Università degli Studi di Torino, Via Pietro Giuria 1, 10125 Torino, Italy
- <sup>92</sup> Department of Physics, Konan University, Kobe, Hyogo, 658-8501, Japan

## Appendix A: Collection area at different stages of the analysis

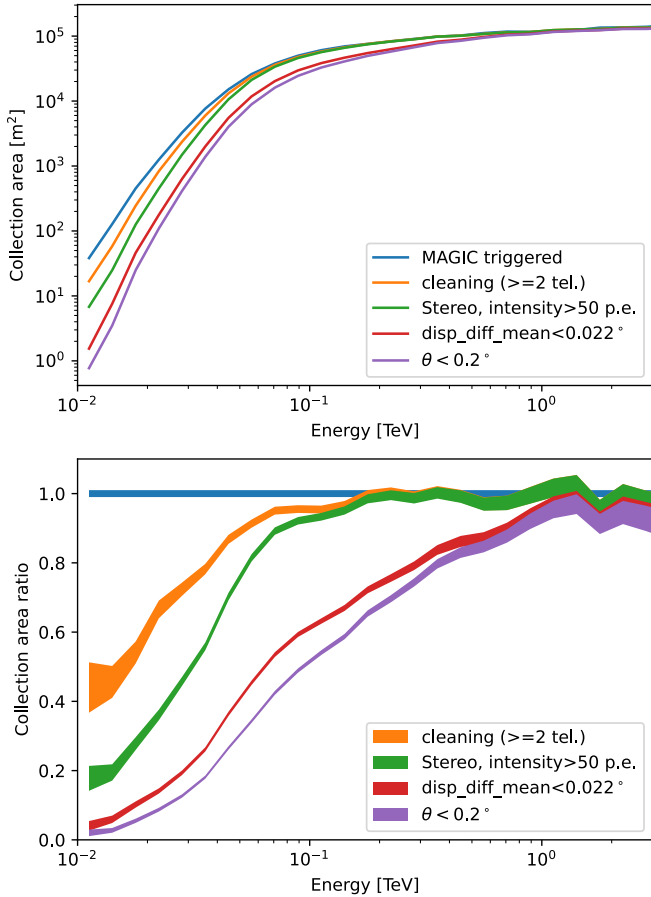


**Fig. A.1.** Collection area at zenith angle of  $10^\circ$  for gamma rays at wobble offset of  $0.4^\circ$  for different stages of analysis: events triggered by both MAGIC telescopes (blue), events with at least two images surviving cleaning (orange), stereoscopic reconstruction with at least two images with intensity above 50 p.e. (green), cut in consistency of reconstructed arrival direction from different images (red), cut in angular distance between the true and reconstructed shower direction (violet). The bottom plot shows the ratio of the collection area at different stages to the MAGIC one at trigger level, with the band width reporting the statistical uncertainty.

In Fig. A.1, we present the changes of the energy-dependent collection area at different analysis stages. Similarly to Abe et al. (2023) a large drop of the collection area at the lowest energies ( $\lesssim 70$  GeV) and the resulting shift of the energy threshold, occurs due to required image cleaning and intensity quality cut. The second quality cut in the agreement of reconstructed positions from different telescopes results in further drop of the collection area, visible up to the level of a few hundred GeVs. Nevertheless, that cut improves considerably angular resolution, such that the effect of the  $\theta < 0.2^\circ$  cut is much milder.

## Appendix B: Validation of the simulation settings

To validate the parameter translation procedure and to assure that the necessary simplifications do not significantly affect the results, a comparison of dedicated MC samples (produced independently with MagicSoft and sim\_telarray) was performed.

For each program we generated<sup>7</sup> 2000 vertical gamma-ray showers of energy 100 GeV, at impact parameters uniformly distributed in the range 30 – 180 m. In Fig. B.1, we present the comparison of true number of p.e. obtained with both chains. The two chains are in agreement with respect to the total observed light yield within  $\sim 2\%$  within the lightpool hump (i.e. for impacts  $\lesssim 120$  m and within 5% in the tail of the shower. Similarly good agreement is also achieved in the trigger efficiency (ratio of triggered and simulated events, see Fig. B.2).

<sup>7</sup> Those special simulations were done not using the array geometry as shown in Fig. 1, but a “virtual” array of MAGIC telescopes located at the distance, 30m, 60m, ..., 180m from a fixed shower axis impact point. For higher impact distances the trigger efficiency drops dramatically.

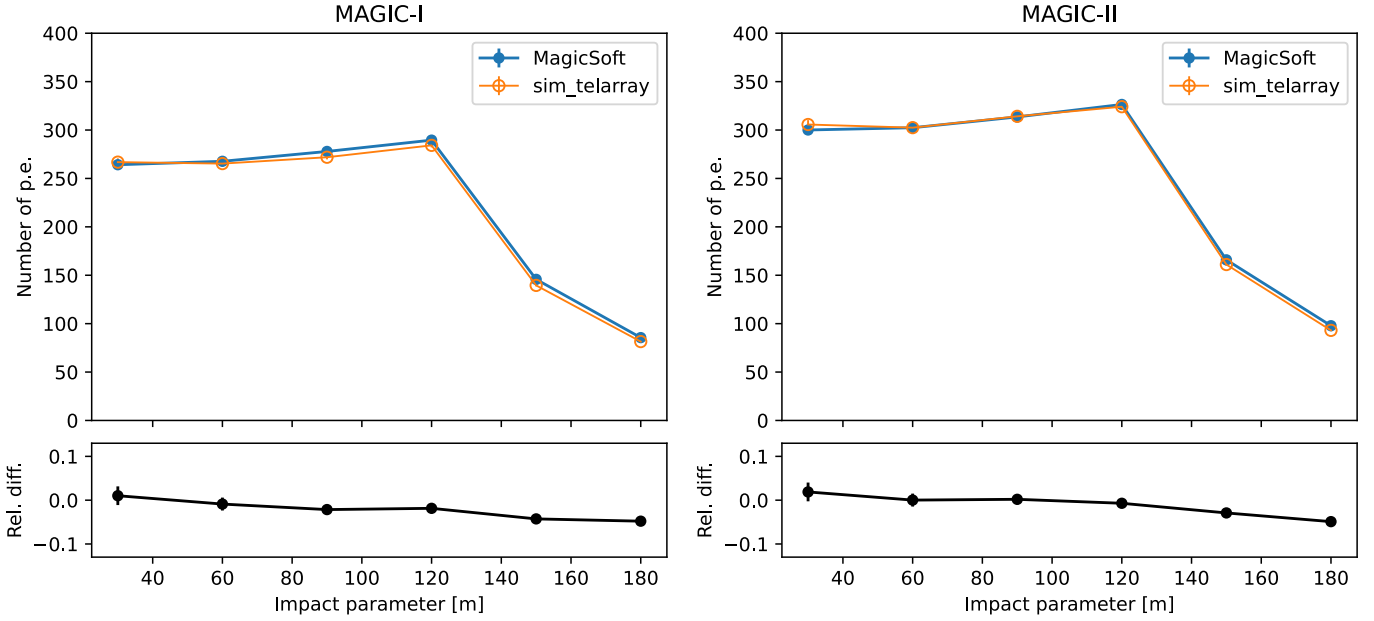


**Fig. B.1.** Comparison of the true number of p.e. obtained with `MagicSoft` (blue) and `sim_telarray` (orange) for 100 GeV gamma rays for MAGIC-I (left) and MAGIC-II (right). In the bottom panel the relative difference of `sim_telarray` with respect to `MagicSoft` is shown.

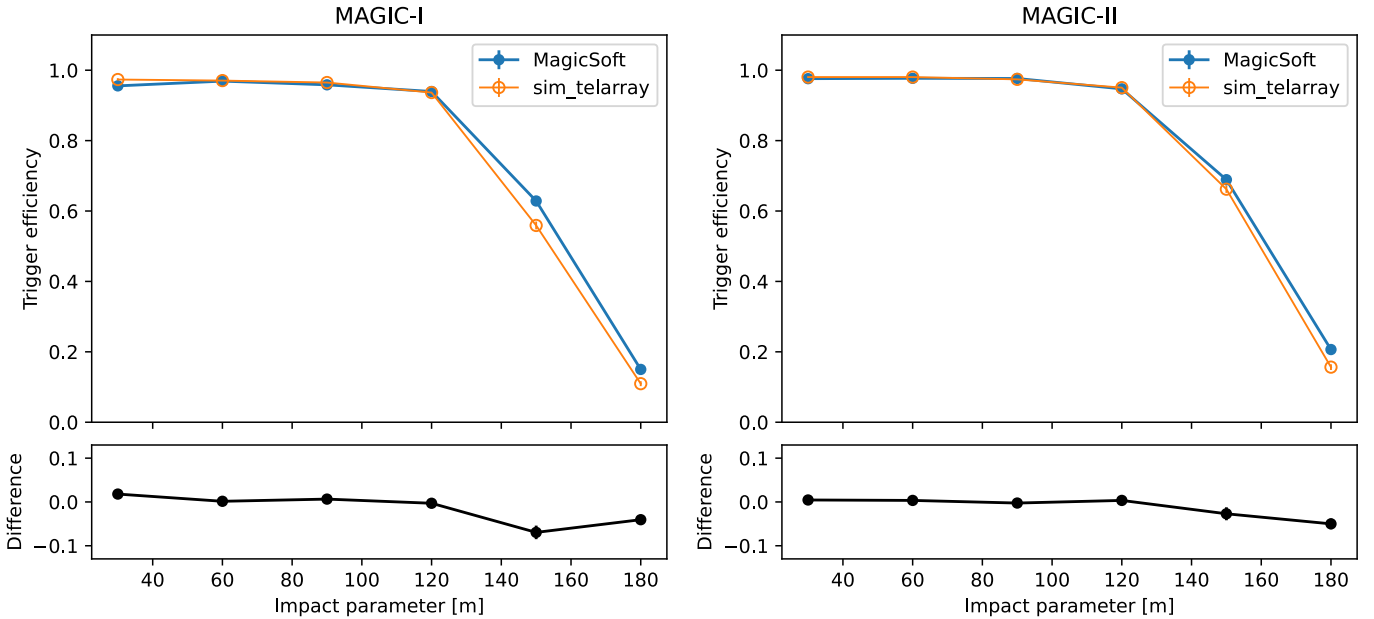


**Fig. B.2.** Comparison of the trigger efficiency obtained with `MagicSoft` (blue) and `sim_telarray` (orange) for 100 GeV gamma rays for MAGIC-I (left) and MAGIC-II (right). In the bottom panel, the difference of `sim_telarray` with respect to `MagicSoft` is shown.

## Appendix C: MAGIC-only performance with MCP

MCP analysis chain can be also applied to MAGIC-only events. Such a use case has limited practical applications because the high level MAGIC-only analysis can also be performed in the CTAO-like framework starting from the so-called DL3 data level (Nigro et al. 2019); however it also turned out to be a useful tool in debugging and comparing the performance of the MAGIC standard chain and MCP. To validate the analysis procedures, we performed such an analysis of a MAGIC Crab Nebula sample. The data were taken on the same nights as the sample used for joint analysis. However, because of lack of the simultaneity condition they amount to a larger duration of 6.6 hrs of effective time (out of which 2.2 hrs are taken in zenith range  $< 30^\circ$

and 3.5 hrs in  $30 - 45^\circ$ ). In Fig. C.1, we compare the energy estimation of the same gamma-like events processed with MCP and with the standard MARS analysis chains. The MCP chain for MAGIC-only analysis uses the same (`sim_telarray`-based) MC simulations as for the joint analysis, however only MAGIC telescopes are selected. There is no visible bias between the two analysis chains: the average energy estimate is consistent within  $\sim 2\%$ .

In Fig. C.2, we present the differential sensitivity comparison with such a data set. In the medium energy range the performance of both chains is similar down to the statistical errors (however a hint of possibly worse performance of MCP is seen at the lowest energies). Comparing the sensitivities computed

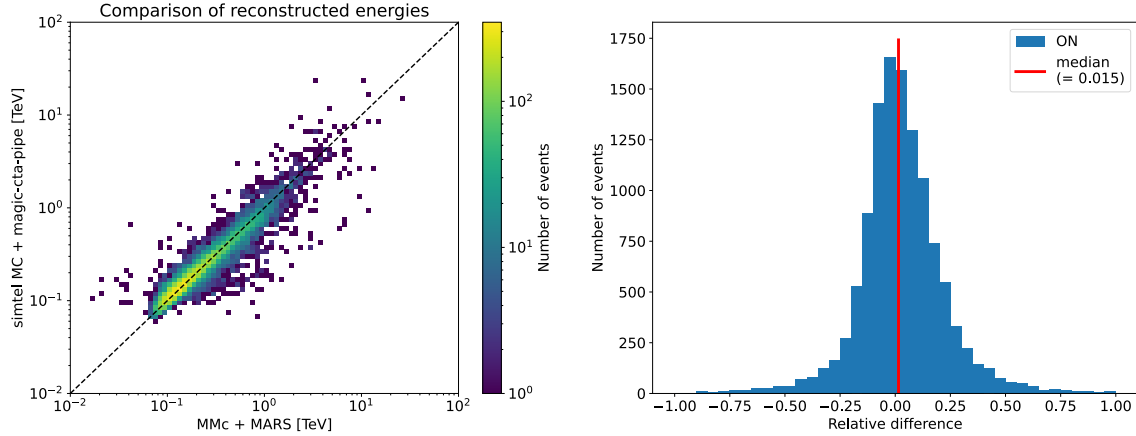


**Fig. C.1.** Comparison of the energy estimate of the same MAGIC-only events with MARS and MCP chain. Left panel: Energy estimated with MCP chain vs energy estimated with MARS. Right panel: Relative difference of MCP-estimated energy with respect to the MARS-estimated one. Only gamma-like events with MARS hadronness value of  $< 0.2$  and intensity of each image above 100 p.e. are used.

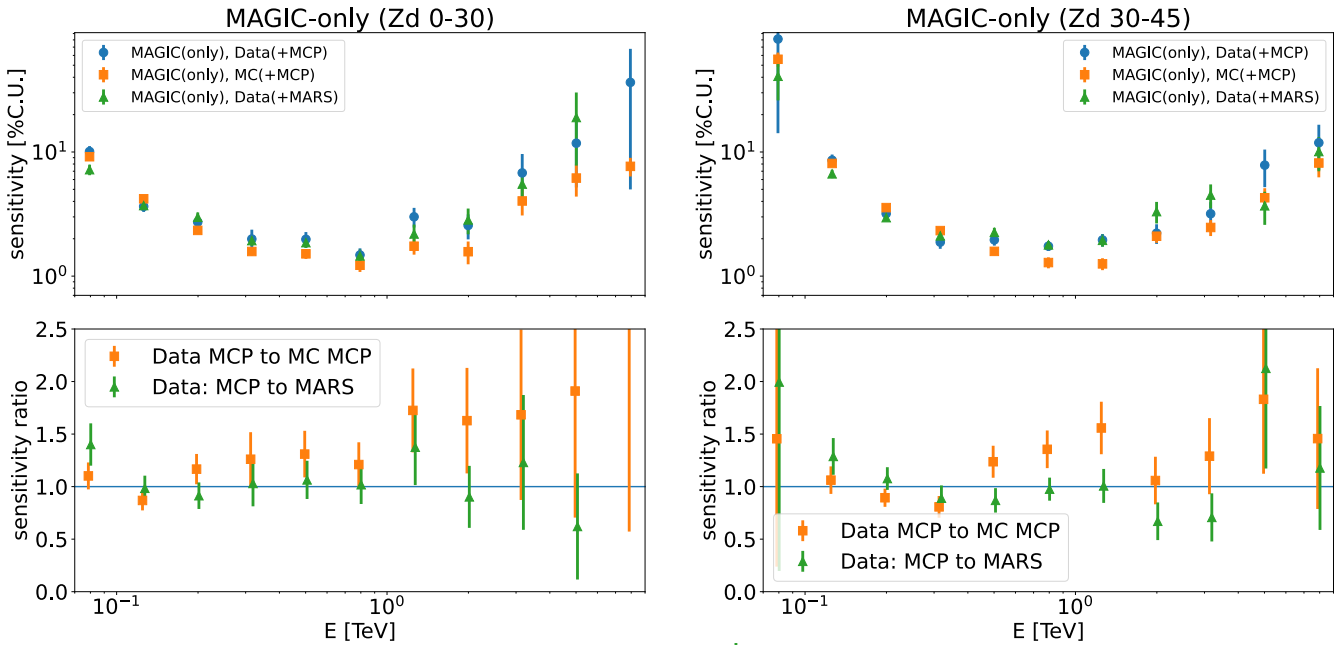


**Fig. C.2.** Differential sensitivity of MAGIC-only observations of MCP analysis chain (blue circles for data and orange squares for MC) compared with the standard MARS analysis over the same data sample (green triangles) for the low-zenith (left) and medium-zenith (right) cases. The bottom panel shows the sensitivity ratios (for visibility of uncertainty bars, the points are shifted in the X axis by  $\pm 1\%$ ).

using the data obtained by observations and MC simulations, the differences for MAGIC-only analysis are typically  $\sim 20 - 30\%$ , except at the highest energies for low-zenith case, where the MC sensitivity uncertainty is very large. Similar differences at mid energies between the data and MC are also reported in the integral sensitivity of [Aleksić et al. \(2012\)](#).

#### Appendix D: Data and MC comparisons with background events

Similarly to the comparisons using the gamma-ray excess, we also compared the bulk of the observed events (cosmic ray background) with the MC simulations. While such a comparison is less sensitive to the optical telescope parameters, it is more direct as it does not require any preselection of events. The results of the comparisons are shown in Fig. D.1. The main contribution in the background events before gamma-selection cuts is

caused by protons, for which we adopted the spectrum from [Yue et al. \(2019\)](#). However, we also take into account helium (with a correction for heavier elements; see Section 4.3 for details) and electrons. Only events with reconstructed direction within  $1^\circ$  from the camera center are used. Moreover, to avoid contamination from the Crab Nebula gamma rays, a region with a radius of  $0.2^\circ$  around the nominal source position has been excluded. We also excluded MAGIC-only events without an LST-1 counterpart. The obtained normalization of the distributions is in agreement with the cosmic-ray measurements. The applied cut for the intensity of  $> 50$  p.e. is sufficient to reproduce properly the intensity distribution of both MAGIC telescopes. In the case of LST-1 however a slight mismatch  $\lesssim 80$  p.e. is visible, which was also reported in [Abe et al. \(2023\)](#) and explained as an effect of less stable trigger thresholds in the data until August 2021. Both the width and length parameter distributions are closely matching between the data and MC simulations. The

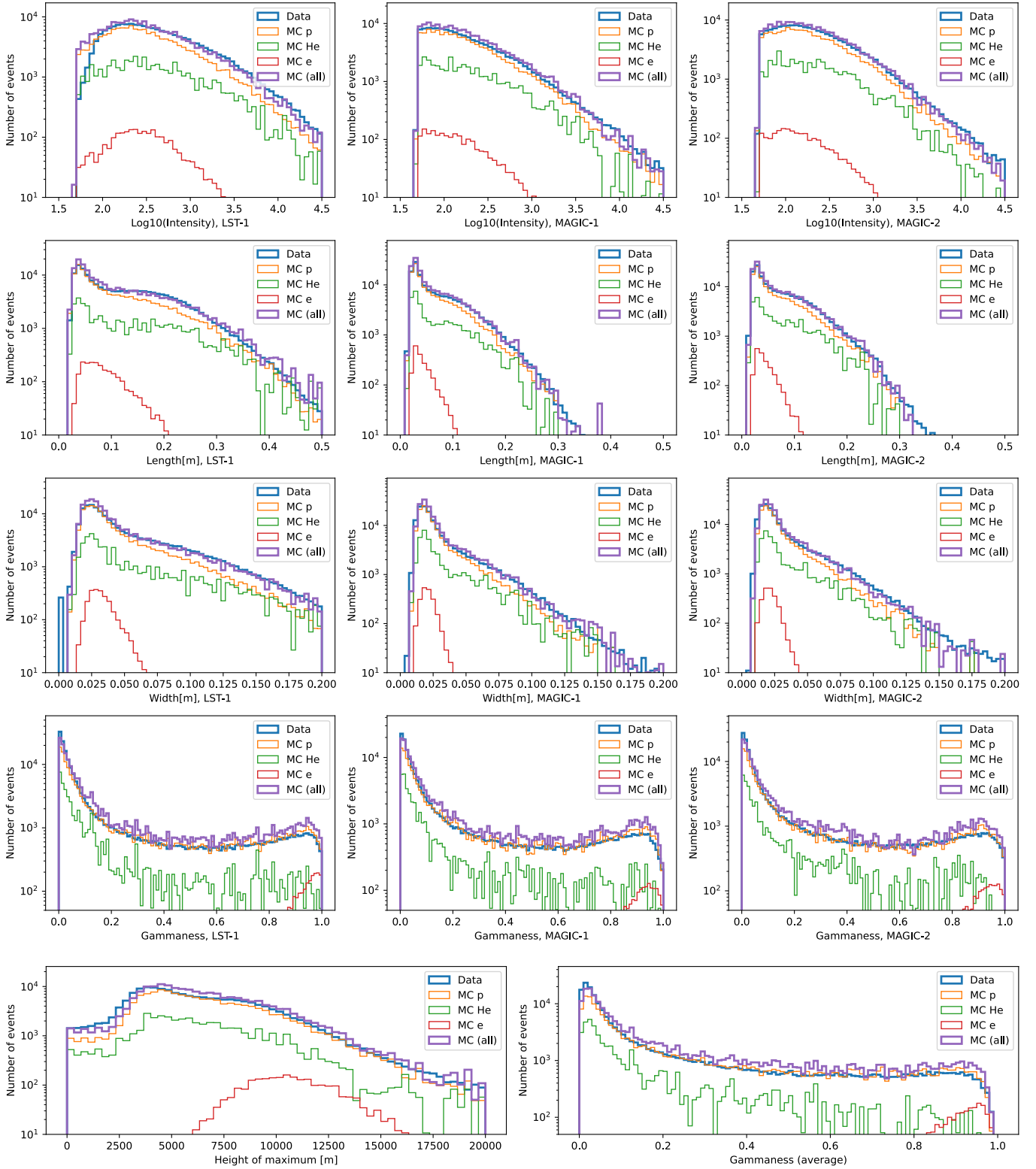


**Fig. D.1.** Comparison of image parameters between the Data and MC simulations (for zenith distance below  $30^\circ$ ). Top four rows of panels show intensity, length, width, and individual telescope “gammaness” (from top to bottom) for LST-1 (left), MAGIC-1 (middle) and MAGIC-II (right). The bottom row shows stereoscopic parameters: height of the shower maximum (left) and averaged “gammaness” (right). In all the panels: the thick blue line shows the data, while the thick magenta line shows the sum of all MC components. Thin lines show the individual components: protons (orange), helium (with an additional correction for heavier elements) (green), and all-electrons (red).

“gammaness” distribution of individual telescopes (as well as the telescopes-averaged values) is relatively well reproduced with

MC simulations. In the case of the height of the shower maximum, the distribution shape is reproduced well, however, a small shift is also present.

## Appendix E: Additional tables

For convenience and possible comparisons with other instruments in this section we report the numerical values of the performance parameters. In Tables E.1 and E.2, we summarize the gamma-ray excess rates, background rates, and derived sensitivity from Crab Nebula data sample and MC simulations. In Fig. E.3, we report the energy resolution derived with different definitions.

$E_0$ [TeV]	Gamma rate (data), [min <sup>-1</sup> ]	Background rate (data), [min <sup>-1</sup> ]	Sensitivity (data) [%C.U.]	Sensitivity (MC) [10 <sup>-12</sup> cm <sup>-2</sup> s <sup>-1</sup> erg]
0.0501	0.27±0.17	0.54±0.11	28.0±19.0	21.1± 2.1
0.0794	2.59±0.34	1.50±0.18	4.81±0.82	4.41± 0.22
0.126	2.68±0.29	0.65±0.12	3.08±0.51	2.41± 0.11
0.2	2.07±0.23	0.272±0.075	2.61±0.54	1.237± 0.089
0.316	2.13±0.21	0.021±0.021	0.77±0.4	0.946± 0.084
0.501	1.23±0.16	0.025±0.010	1.44±0.36	0.882± 0.086
0.794	0.81±0.13	0.0041±0.0017	1.03±0.27	0.610± 0.073
1.26	0.458±0.098	0.0016±0.0011	1.29±0.54	0.537± 0.087
2.0	0.271±0.075	0.00088±0.00088	1.8±1.0	0.69± 0.13
3.16	0.164±0.059	0.0032±0.0023	4.6±2.4	0.82± 0.21
5.01	0.104±0.047	–	3.2±1.4	0.96± 0.32
7.94	0.021±0.021	–	16.0±16.0	0.80± 0.14

**Table E.1.** Rates and sensitivity values for Crab Nebula observations and MC simulations at zenith distance < 30°, as plotted in Figures 7 and 8 (left panels).

*Note:* Rates are integrated in 0.2 decades centered on  $E_0$  value. Data sensitivities are provided in the percentage of Crab Nebula flux, while MC sensitivities in SED units.

$E_0$ [TeV]	Gamma rate (data), [min <sup>-1</sup> ]	Background rate (data), [min <sup>-1</sup> ]	Sensitivity (data) [%C.U.]	Sensitivity (MC) [10 <sup>-12</sup> cm <sup>-2</sup> s <sup>-1</sup> erg]
0.0794	0.59±0.12	0.715±0.072	14.6±3.4	13.0± 0.96
0.126	2.43±0.19	1.42±0.10	4.99±0.51	3.86± 0.16
0.2	2.65±0.15	0.307±0.047	2.16±0.24	1.747± 0.072
0.316	2.03±0.13	0.093±0.026	1.6±0.26	1.206± 0.064
0.501	1.171±0.093	0.0229±0.0057	1.46±0.22	0.798± 0.047
0.794	0.899±0.081	0.0093±0.0016	1.29±0.16	0.595± 0.047
1.26	0.806±0.076	0.0096±0.0016	1.45±0.19	0.458± 0.048
2.0	0.319±0.048	0.00264±0.00076	2.21±0.46	0.458± 0.062
3.16	0.185±0.036	0.0007±0.00049	2.46±0.99	0.525± 0.089
5.01	0.113±0.029	0.00138±0.00056	5.0±1.6	0.67± 0.15
7.94	0.084±0.025	0.00148±0.00086	6.8±2.9	0.70± 0.20

**Table E.2.** As in Table E.1 but for zenith distance 30 – 45° (see also Figures 7 and 8, right panels).

E [TeV]	Res. 68% [%]	Res. (S.D.) [%]	Res. (fit) [%]
0.0794	19.2±0.1	20.27±0.06	16.16±0.05
0.126	16.26±0.07	17.32±0.04	15.63±0.04
0.2	15.83±0.08	16.82±0.04	15.34±0.04
0.316	14.68±0.08	15.91±0.04	14.5±0.04
0.501	13.82±0.08	15.7±0.05	13.99±0.04
0.794	13.54±0.09	16.24±0.06	13.84±0.05
1.26	13.5±0.1	17.32±0.07	13.87±0.06
2.0	13.3±0.1	18.18±0.09	13.57±0.07
3.16	12.7±0.1	19.5±0.1	13.63±0.08
5.01	13.9±0.2	20.9±0.2	14.4±0.1
7.94	15.6±0.3	20.4±0.2	15.0±0.1
12.6	15.9±0.4	20.4±0.2	15.2±0.2

**Table E.3.** Energy resolution at zenith distance 23.6° corresponding to Fig. 12.

*Note:* The columns report: true energy, 68% containment resolution, standard deviation (S.D.), and tail-less fit.